

Supporting information

Molecular Design of High-performance Wide-bandgap Acceptor Enables Versatile Organic Photovoltaic Applications

Yang Xiao,^{a,b} Jingwen Wang,^{a,b} Yong Cui,^{a} Yafei Wang,^{a,b} Zhihao Chen,^a
Shuohan Cheng,^{a,b} Haoyu Yuan,^c Jiawei Qiao,^d Yi Yang,^{a,b} Wenxuan
Wang,^{a,b} Ni Yang,^{a,b} Yue Yu,^{a,b} Runnan Yu,^c Xiaotao Hao,^d and Jianhui
Hou,^{a,b*}*

^aState Key Laboratory of Polymer Physics and Chemistry, Beijing National Laboratory for Molecular Sciences, Institute of Chemistry, Chinese Academy of Sciences, Beijing 100190, P. R. China.

^bUniversity of Chinese Academy of Sciences, Beijing 100049, P. R. China.

^cCollege of Materials Science and Engineering, Beijing University of Chemical Technology, Beijing 100029, P. R. China.

^dSchool of Physics, State Key Laboratory of Crystal Materials, Shandong University, Jinan, Shandong 250100, P. R. China

Corresponding Author: ycui1990@iccas.ac.cn; hjhzlz@iccas.ac.cn

Materials

Compound 2-3, PBQx-TF, and NDI-Ph were purchased from Solarmer Materials Inc. PEDOT:PSS, Clevios™ P VP AI 4083, was purchased from Heraeus. The other reagents and solvents were commercially available and purchased from J&K chemicals, Innochem, Sinopharm Chemical Reagent Co, Ltd and Bei Jing TongGuang Fine Chemicals Company, and these reagents and solvents were used without further purification.

Materials characterization

¹H-, ¹³C-NMR spectra were recorded on Bruker Fourier 300 or Avance III 400 HD spectrometer. Matrix Assisted Laser Desorption Ionization Time of Flight Mass Spectrometry (MALDI-TOF-MS) was measured with a Bruker Reflex II-TOF spectrometer.

Ultraviolet-visible (UV-Vis) absorption spectra in solution and in solid films were measured using Hitachi UH5300 UV-vis spectrophotometer. The solid film samples were spin-coated with chloroform solution of the acceptors (ITCC-Cl, FPCC-Cl, and FPCC-Br, 15mg/ml) or toluene solution of donor (PBQx-TF, 7.5 mg/mL) on the quartz plates. The film thickness was obtained via a surface profilometer (Dektak XT, Bruker). The molecular energy levels were measured by CHI650D electrochemical workstation with three-electrode cell in anhydrous acetonitrile solvents solution of Bu₄NPF₆ (0.1 M) with scanning rate of 0.05 V·s⁻¹ under argon atmosphere. Ferrocene/ferrocenium (Fc/Fc⁺) was used as an external standard in the measurement.

Morphology characterization

Atomic force microscope (AFM) images were recorded on Bruker Nanoscope V AFM microscope by tapping mode. The transmission electron microscope (TEM) images of the blend films were obtained by a (JEOL) JEM-2200FS electron microscope with an accelerating voltage of 200 kV. The GIWAXS data were obtained at 1W1A Diffuse X-ray Scattering Station, Beijing Synchrotron Radiation Facility (BSRF-1W1A). The samples were prepared by spin-coating onto Si substrates.

Theoretical calculation

The theoretical calculations, including electrostatic potential (ESP), highest occupied molecular orbital (HOMO) level and lowest unoccupied molecular orbital (LUMO) levels, were conducted using the Gaussian 09 program based on the density functional theory method using B3LYP/6-31G (d, p). The exchange integral between HOMO LUMO distribution and local electron attachment energies (LEAE) were calculated by Gaussian 09 program and analyzed by Multiwfn software.

Femtosecond transient absorption (TA) spectra

Femtosecond transient absorption (TA) spectra were measured on an Ultrafast Helios pump-probe system in collaboration with a regenerative amplified laser system from Coherent. The pulses with a repetition rate of 1kHz, a length of 100 fs, and an energy of 7 mJ/pulse, were generated by a Ti:sapphire amplifier (Astrella, Coherent). Then the pulses were separated into two parts by a beam splitter. One part was coupled into an optical parametric amplifier (TOPAS, Coherent) to generate the pump pulses at 400 and 700 nm. The other part was focused onto a sapphire plate and a YAG plate to generate white light supercontinuum as the probe beams with spectra covering 420-800 nm and 750-1600 nm, respectively. The time delay between pump and probe was controlled by a motorized optical delay line with a maximum delay time of 8 ns. The sample films were spin-coated onto the 1 mm-thick quartz plates and encapsulated by epoxy resin in nitrogen-filled glove box to resist water and oxygen in the air. The pump pulse is chopped by a mechanical chopper with 500 Hz and then focused on to the mounted sample with probe beams. The probe beam was collimated and focused into a fiber-coupled multichannel spectrometer with CCD sensor. The energy of pump pulse was measured and calibrated by a power meter (PM400, Thorlabs).

Temperature depended photoluminescence (PL) spectra

The PL spectra were recorded using a fiber-connected spectrometer (DU420A-OE, ANDOR). The pump power density was maintained at a constant value of 5 $\mu\text{J cm}^{-2}$. For the temperature depended PL measurements, the sample temperature was

controlled by Model 325 Cryogenic Temperature Controller (Lake Shore Cryotronics, Inc.) in a Liquid nitrogen thermostatic chamber. All samples were fabricated on Si substrates.

Device fabrication

The OPV devices were fabricated with a structure of ITO/PEDOT: PSS/active layer/NDI-Ph/Ag. ITO glass ($6\Omega\text{ cm}^{-2}$) was purchased from South China Xiang's Science & Technical Company Limited. PEDOT: PSS (4083) was purchased from the CleviosTM. PEDOT: PSS was diluted with the same volume of water. NDI-Ph was purchased from Solarmer Material Inc. The ITO glasses were treated with ultraviolet-ozone for 10 min. Afterward, about 10 nm PEDOT: PSS was spin-coated on the ITO glass at 3000 r.p.m. for 30 s. Subsequently, the ITO glasses were treated by thermal annealing for 15 min at 150°C. Then, the substrates were transferred to a glove box. PBQx-TF: ITCC-Cl, PBQx-TF: FPCC-Cl, and PBQx-TF: FPCC-Br with a weight ratio of 1:1.2 were dissolved in toluene at a polymer concentration of 6 mg mL^{-1} . The active layer solutions need to be stirred at 90°C until completely dissolved. 0.5% 1,8-diiodooctane (DIO) (v/v) was added to the solutions 30 min before the spin-coating process. The active layer solutions were spin-coated onto the PEDOT: PSS layers at 5000 r.p.m. for 30 s. The best active layer thickness is about 100 nm. Then, the films were treated with thermal annealing at 120°C for 10 min. NDI-Ph was dissolved in methanol at a concentration of 1.5 mg mL^{-1} at 50°C and then spin-coated on the top of the active layers at 3000 rpm for 30 s with a thickness about 15 nm. Finally, 100 nm Ag was deposited under a high vacuum ($\sim 9\times 10^{-4}\text{ Pa}$). The prepared device is encapsulated with epoxy resin in a glove box under a nitrogen atmosphere and then applied for indoor lighting and underwater photovoltaic testing.

The SCLC devices have same active layers while containing different electrodes and charge transfer layers with structures of ITO/ZnO/active layers/Al for the electron-only devices and ITO/MoO₃/active layers/Au for the hole-only devices.

Fabrication of tandem photovoltaic cells

Photovoltaic cells were fabricated with the inverted structure (ITO/ZnO NPs/front subcell/MoO₃/ultrathin Ag/ZnO-NPs+PFN-Br/rear subcell/MoO₃/Ag). Firstly, about

10 nm ZnO layers were spin-coated on the pre-cleaned ITO substrates and annealed at 100°C for 10 min. Then, PBQx-TF:FPCC-Br layer was spin-coated. Then 15 nm MoO₃ and 1 nm ultra-thin Ag layer were evaporated under high vacuum. Subsequently, the ZnO nano particles (NPs) and PFN-Br colloidal solution was casted on the front cells and annealed at 100°C for 3 min. After that, the solution of PBDB-TF:BTP-eC9:HDO-4Cl was spin-coated. Finally, 8 nm MoO₃ and 150 nm Ag were evaporated on top of rear active layer.

Device characterization and measurement

J - V measurements were performed using solar simulator (SS-F5-3A, Enli Technology Co. Ltd.) with AM 1.5G spectra (100 mW cm⁻²). The J - V curves of the cells submerged in water at different depths are obtained by first calibrating the light source to AM 1.5G and then immersing the cells in water for measurement. Exciton dissociation was also determined by measuring J_{ph} - V_{eff} curve. J_{ph} is defined as $J_{ph} = J_L - J_D$, where J_L and J_D stand for the current density under illumination and in dark, respectively. The V_{eff} is defined as $V_{eff} = V_0 - V$, where V_0 is voltage when the J_{ph} is zero, V is the applied voltage. The J_{sat} is the saturation photocurrent density. The exciton dissociation probability (P_{diss}) is calculated from the equation $P_{diss} = J_{ph}/J_{sat}$. The external quantum efficiency (EQE) tests were measured by using an integrated IPCE measurement system of QE-R3011 (Enli Technology Co. Ltd.). Electroluminescence quantum efficiencies (EQE_{EL}) were measured by applying external voltage/current sources through the devices using Enlitech ELCT-3010. All devices used in EQE_{EL} were prepared under optimal device fabrication conditions. Photo-induced charge carrier extraction by linear increasing voltage (photo-CELIV) measurement was carried on an all-in-one characterization platform Paios developed and commercialized by Fluxim AG, Switzerland. Highly sensitive EQE was obtained with an integrated system (PECT-600, Enli Technology Co. Ltd.).

Calculation of spectral irradiance at different depths underwater

The spectral irradiance at different depths of water were obtained through the spectral irradiance of AM1.5 G and the absorption coefficient of pure water, which can be calculated as:

$$P(x, \lambda) = P(0, \lambda)e^{-\alpha x}$$

Where $P(x, \lambda)$ is the spectral irradiance of different water depths, $P(0, \lambda)$ is the spectral irradiance of AM 1.5G, α is the absorption coefficient of pure water, and x is the depth of water.

Voltage loss analysis

The voltage loss (ΔV_{loss}) can be converted into energy loss ($\Delta E_{\text{loss}} = q\Delta V_{\text{loss}}$) and can be split into three parts:

$$\begin{aligned} \Delta V_{\text{loss}} &= E_g/q - V_{\text{OC}} \\ &= \left(\frac{E_g}{q} - V_{\text{OC}}^{\text{SQ}} \right) + (V_{\text{OC}}^{\text{SQ}} - V_{\text{OC}}^{\text{rad}}) + (V_{\text{OC}}^{\text{rad}} - V_{\text{OC}}) = \Delta V_1 + \Delta V_2 + \Delta V_3 \end{aligned} \quad (1)$$

The E_g value is determined by the derivatives of the Fourier transform photocurrent spectroscopy. $V_{\text{OC}}^{\text{SQ}}$ is the maximum voltage based in the Shockley-Queisser (SQ) limit, where the EQE_{PV} is assumed to be a step-function:

$$\text{EQE}_{\text{PV}}(E) = 1, (E \geq E_g); \text{EQE}_{\text{PV}}(E) = 0, (E \leq E_g) \quad (2)$$

Then, $V_{\text{OC}}^{\text{SQ}}$ can be calculated using the following equation:

$$V_{\text{OC}}^{\text{SQ}} = \frac{k_{\text{B}}T}{q} \ln \left(\frac{J_{\text{SC}, \text{SQ}}}{J_{0, \text{SQ}}} + 1 \right) = \frac{k_{\text{B}}T}{q} \ln \left(\frac{q \int_{E_g}^{\infty} \phi_{\text{AM1.5}}(E) dE}{q \int_{E_g}^{\infty} \phi_{\text{bb}}(E) dE} + 1 \right) \quad (3)$$

where $\phi_{\text{AM1.5}}$ is the solar radiation photon flux, ϕ_{bb} is the black body radiation at 300 K. $V_{\text{OC}}^{\text{rad}}$ is the voltage that only exists in radiative recombination, determined by the formula:

$$V_{\text{OC}}^{\text{rad}} = \frac{k_{\text{B}}T}{q} \ln \left(\frac{J_{\text{SC}}}{J_{0, \text{rad}}} + 1 \right) = \frac{k_{\text{B}}T}{q} \ln \left(\frac{q \int_0^{\infty} \text{EQE}_{\text{PV}} \phi_{\text{AM1.5}}(E) dE}{q \int_0^{\infty} \text{EQE}_{\text{PV}} \phi_{\text{bb}}(E) dE} + 1 \right) \quad (4)$$

The voltage loss due to non-radiative recombination can be obtained by:

$$\Delta V_3 = \Delta V_{\text{OC}}^{\text{non-rad}} = V_{\text{OC}}^{\text{rad}} - V_{\text{OC}} = -\frac{k_{\text{B}}T}{q} \ln(\text{EQE}_{\text{EL}}) \quad (5)$$

Stability measurement

After the encapsulated device is continuously heated at 80°C, the thermal stability of the PCE of device at 80°C is measured under the AM 1.5G condition.

Indoor measurements

For indoor measurements, the light-emitting diode (LED) light source (2700 K) was used. Spectrometer HS-IL (Enli Technology Co., Ltd., Taiwan) is used to calibrate the spectral irradiance. The spectrometer is calibrated by Enli Tech. Optoelectronic Calibration Lab. at 2021/08/13 (Report No. PVS210801), following standards: American Society of Testing and Materials ASTM G-138-12 “Standard Test Method for Calibration of a Spectrometer Using a Standard Source of Irradiance”. For intensity calibration, the illuminance and emission spectra are measured just below the LED source (the position of OPV cells) via the spectrometer. The illuminance variation is realized by changing the distance from light source. Then, the light intensity is calculated by integrating the emission spectra with the wavelength. For the $J-V$ measurements under indoor lighting, the OPV cells are placed just below the LED source and their $J-V$ curves are harvested by using Keithley 2400. The area of OPV cells used in indoor measurements is 0.39 cm² because large device area can effectively suppress the edge effect to avoid the overestimation of device performance under weak illuminance and diverging light. The EQE value at different wavelengths represents the conversion efficiency from photon to electron at corresponding wavelength. The integrated current density (J_{cal}) is calculated from the corresponding EQE spectra based on the following equation:

$$J_{\text{cal}} = \frac{q}{hc} \int \phi(\lambda) \text{EQE}(\lambda) \lambda d\lambda$$

where q is the elementary charge, $\phi(\lambda)$ is the emission spectrum of light source, λ is wavelength, h is Planck constant, c is light velocity. If the EQE spectra is fixed, the J_{cal} will only relate to the emission spectrum of light source.

Photovoltaic electrolysis experiment

A 1 cm² FPCC-Br-based organic photovoltaic (OPV) cell was fabricated by blade-coating for underwater photovoltaic electrolysis. Prior to conducting underwater electrolysis experiments, all devices were encapsulated using epoxy resin and glass. Initially, copper tapes and wires were used to create external circuit connections to the electrode tabs. Subsequently, a ring of epoxy resin was applied around the active area of the silver electrode side of the cell. A piece of glass, cut to match the cell's dimensions, was placed atop the epoxy resin. The epoxy was then cured under exposure to 365 nm UV light for 15 minutes to ensure complete polymerization. The resulting encapsulated cells are suitable for long-term storage and application in underwater photovoltaic electrolysis.

The linear sweep voltammetry (LSV) curve was obtained using a two-electrode system (two platinum strip electrodes) with a scan rate of 10 mV/s. Subsequently, a cell was connected in series to the circuit to investigate the reduction of overpotential. Two 1 cm² FPCC-Br-based cells, when connected in series, can directly perform underwater photovoltaic electrolysis. Chronoamperometric tests were conducted by immersing the two series-connected organic photovoltaic cells 5 cm underwater, with a test bias of 0 V. The electrolyte for all electrolysis conditions is a 1M KOH solution, and the anode and cathode for electrolysis are both platinum electrodes.

Efficiency prediction of underwater photovoltaics

According to the basic assumption of Shockley-Queisser (SQ), the power conversion efficiency (PCE) of photovoltaic cells is the ratio of maximum output power (P_{\max}) to incident light power (P_{in}), as follows:

$$\text{PCE} = \frac{P_{\max}}{P_{\text{in}}} \times 100\% = \frac{V_{\text{OC}} \times J_{\text{SC}} \times \text{FF}}{P_{\text{in}}} \times 100\% \quad (6)$$

where V_{OC} is the open circuit voltage, J_{SC} is the short circuit current, and FF is the Fill Factor. The V_{OC} is determined by the following formula (7):

$$qV_{\text{OC}} = E_{\text{g}} - E_{\text{loss}} \quad (7)$$

Where q is the elemental charge, E_{g} is the optical bandgap of device, E_{loss} is the energy loss (assuming that $E_{\text{loss}} = 0.5$ eV). The J_{SC} can be estimated by multiplying the photon flux $N(\lambda)$ over the entire absorption range by the external quantum efficiency (EQE)

value, where the EQE value is assumed to be 90%:

$$J_{sc} = q \int_0^{\lambda} N(\lambda)EQE(\lambda)d\lambda = q \int_0^{\lambda} 0.9 \times N(\lambda)d\lambda \quad (8)$$

Subsequently, FF can be determined by a semi-empirical formula:

$$FF = \frac{v_{oc} - \ln(v_{oc} + 0.72)}{v_{oc} + 1} - 0.1 \quad (9)$$

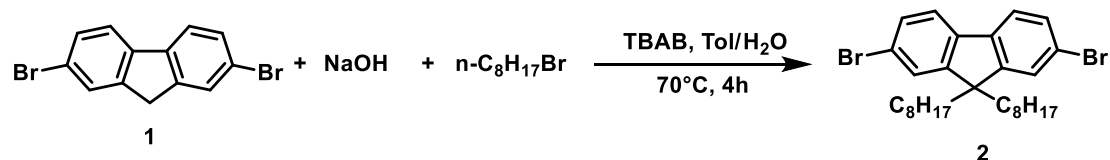
$$v_{oc} = \frac{qV_{oc}}{nkT} \quad (10)$$

Where n is the ideal factor and is assumed to be 1.

Synthetic details

Compound 2-4 can be synthesized according to previous literature^[1, 2].

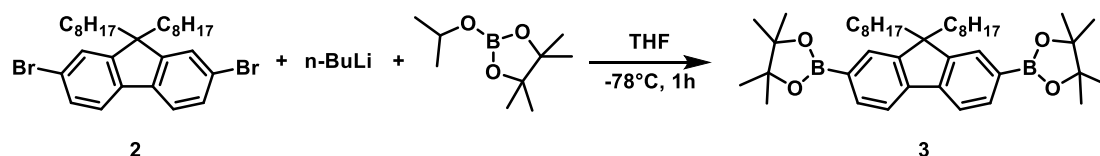
2,7-dibromo-9,9-dioctyl-9H-fluorene (compound 2)



In a 1 L of two-neck round bottom flask, compound 1 (100 g, 310 mmol) and 1-bromooctane (125 g, 650 mmol) were dissolved in 450 mL of mixed solvent (toluene: water =300: 150 mL), and then the two-neck round bottom flask was incubated in an ice bath to 0 °C. After slowly adding sodium hydroxide (26 g, 650 mmol), the ice bath was removed and the reaction was kept at room temperature. Afterwards, tetrabutylammonium bromide (3.0 g, 10 mmol) was added to the reaction flask and the flask was heated to 70 °C. After 4 hours, the reaction was cooled to room temperature. Separate the organic and aqueous phases using a separatory funnel, and extract the aqueous phase with dichloromethane (100 mL × 3). The solvent was removed under vacuum and the residue was purified by silica gel column using petroleum ether as eluent. The product compound 2 was obtained as white solid (151.3 g, 89%). ¹H NMR (300 MHz, Chloroform-*d*) δ 7.51 (d, $J = 8.6$ Hz, 2H), 7.49 – 7.41 (m, 4H), 1.99 – 1.83

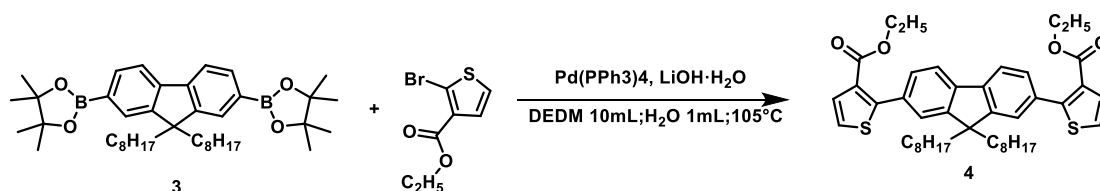
(m, 4H), 1.06 (t, $J = 3.5$ Hz, 20H), 0.83 (t, $J = 6.9$ Hz, 6H), 0.58 (t, $J = 6.5$ Hz, 4H). MS (MALDI-TOF): m/z Calcd. for $C_{29}H_{40}Br_2$: 548.15 [M], Found 547.89 [M]⁺.

2,2'-(9,9-dioctyl-9H-fluorene-2,7-diyl)bis(4,4,5,5-tetramethyl-1,3,2-dioxaborolane)
(**compound 3**)



In a 1 L of two-neck round bottom flask, compound 2 (100 g, 182.3 mmol) was dissolved in 500 mL of dry tetrahydrofuran under an inert atmosphere, and then the solution was cooled down to -78°C . After that, n-Butyl lithium (n-Buli, 2.5 M, 160 mL, 401 mmol) was added into the flask dropwise. The mixture was slowly warmed to not more than -50°C and stirred for 1 hour until 2-isopropoxy-4,4,5,5-tetramethyl-1,3,2-dioxaborolane (82.8 g, 445 mmol) was added into the flask in one portion. Then, the reaction was cooled to -78°C . Subsequently, the mixture was slowly warmed to room temperature and stirred for another 1 hour. The solvent was removed under vacuum and the residue was extracted with hot water at 60°C and ethyl acetate. The organic phase was removed under vacuum and recrystallization was carried out using n-octane and n-butanol by turn. The product compound 3 was obtained as white crystal (92.5 g, 79%). ¹H NMR (300 MHz, Chloroform-d) δ 7.80 (dd, $J = 7.5, 1.0$ Hz, 2H), 7.77 – 7.67 (m, 4H), 2.05 – 1.93 (m, 4H), 1.39 (s, 24H), 1.23 – 0.94 (m, 20H), 0.80 (t, $J = 7.0$ Hz, 6H), 0.54 (s, 4H).

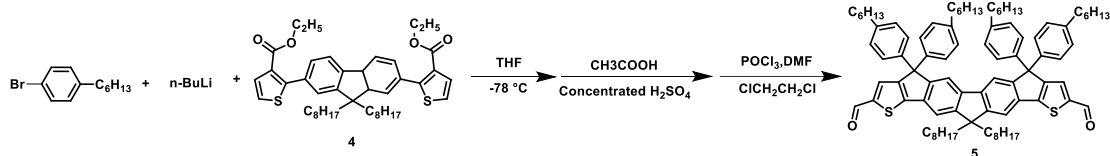
diethyl 2,2'-(9,9-dioctyl-9H-fluorene-2,7-diyl)bis(thiophene-3-carboxylate)
(**compound 4**)



In a 100 mL of two-neck round bottom flask, compound 3 (1.50 g, 2.32 mmol), ethyl 2-bromothiophene-3-carboxylate (1.2 g, 5.1 mmol), lithium hydroxide monohydrate (214 mg, 5.1 mmol) and Pd (PPh₃)₄ (54 mg, 0.0464 mmol) were dissolved into mixed

solvent (Diethylene glycol dimethyl ether (DEDM): water =10: 1 mL) under inert atmosphere, and the reaction was stirred overnight at 105 °C. After removing the solvent under vacuum, the residue was purified by silica gel column chromatography using CH₂Cl₂/PE (1:1) as eluent. Finally, the orange-yellow solid (compound 4) was obtained with a yield of 86%. ¹H NMR (300 MHz, Chloroform-*d*) δ 7.72 (d, *J* = 7.8 Hz, 2H), 7.56 – 7.39 (m, 6H), 7.25 (s, 2H), 4.19 (q, *J* = 7.1 Hz, 4H), 1.27 – 1.00 (m, 28H), 0.80 (t, *J* = 6.9 Hz, 12H). MS (MALDI-TOF): *m/z* Calcd. for C₄₃H₅₄O₄S₂: 698.35 [M], Found 698.00 [M]⁺.

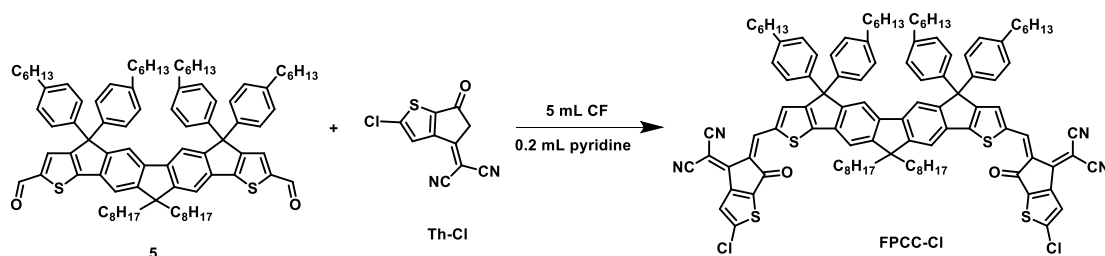
Compound 5



In a 100 mL of two-neck round bottom flask, 1-bromo-4-hexylbenzene (2.52 g, 10.44 mmol) was dissolved in THF under inert atmosphere, and the reaction was stirred overnight at -78 °C. After that, n-Butyl lithium (n-Buli, 2.5 M, 4.2 mL, 10.44 mmol) was added into the flask dropwise. The mixture was slowly warmed to not more than -50°C and stirred for 1 hour until compound 4 (1.824 g, 2.61 mmol) was added into the flask in one portion. Before quenching with methanol, the reaction is naturally warmed to room temperature and stirred for 1 hour. After adding 100 mL of water to the reaction solution, the aqueous phase was extracted with 3 * 100 mL of ethyl acetate, and finally dry the organic phase with magnesium sulfate. After removing the solvent from the organic phase under vacuum, dissolve the residue in 20mL of acetic acid and add 4 drops of concentrated sulfuric acid. After stirring at 120 °C for 1 hour in an inert atmosphere, the reaction was quenched by adding 50 mL of water. Then, the aqueous phase was extracted with 3 * 100 mL of dichloromethane, and finally dry the organic phase with magnesium sulfate. After removing the solvent from the organic phase under vacuum, dissolve the residue in 10mL of 1,2-Dichloroethane. During this period, prepare a 100mL two necked reaction flask and create an inert atmosphere.

Subsequently, at 0 degrees Celsius, 5 mL of POCl₃ and DMF were sequentially added to the bottle and reacted for 0.5 hours. After that, the 1,2-dichloroethane solution of the above residue was added to the reaction flask. Then, the reaction was stirred overnight at 80 °C. After the reaction is complete, the reaction solution is added dropwise to 500 mL of 0.1 M NaOH solution and stirred for 4 hours. Then, the aqueous phase was extracted with 3 * 100 mL of dichloromethane, and finally dry the organic phase with magnesium sulfate. After removing the solvent under vacuum, the residue was purified by silica gel column chromatography using CH₂Cl₂/PE (1:1) as eluent. Finally, the orange-yellow solid (compound 5) was obtained with a yield of 60%. ¹H NMR (400 MHz, Chloroform-*d*) δ 9.83 (s, 2H), 7.64 (s, 2H), 7.57 (d, *J* = 0.7 Hz, 2H), 7.52 (d, *J* = 0.6 Hz, 2H), 7.12 (d, *J* = 8.4 Hz, 8H), 7.07 (d, *J* = 8.5 Hz, 8H), 2.63 – 2.44 (m, 8H), 2.11 – 1.97 (m, 4H), 1.54 (s, 10H), 1.38 – 1.22 (m, 24H), 1.09 (s, 20H), 0.86 (s, 12H), 0.78 (s, 10H). MS (MALDI-TOF): *m/z* Calcd. for C₈₉H₁₁₀O₂S₂: 1274.79 [M], Found 1275.07 [M]⁺.

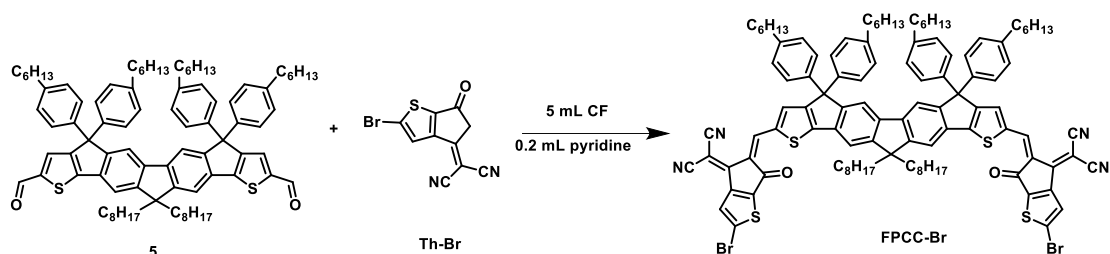
FPCC-Cl



In a 50 mL of two-neck round bottom flask, compound 5 (200mg, 0.157 mmol) and Th-Cl (183.9 mg, 0.784 mmol) were dissolved in 5 mL of CHCl₃, and then 0.20 mL of pyridine was added into the mixture by syringe. The reaction was stirred at room temperature overnight. The solvent was removed under vacuum and the residue was purified by silica gel column using CHCl₃ as eluent. The product FPCC-Cl was obtained as blue black solid (201 mg, 75%). ¹H NMR (400 MHz, Chloroform-*d*) δ 8.62 (s, 1H), 8.60 (s, 1H), 7.85 (s, 1H), 7.63 (s, 4H), 7.59 (s, 2H), 7.29 (s, 1H), 7.10 (q, *J* = 8.3 Hz, 16H), 2.55 (t, *J* = 7.8 Hz, 8H), 2.05 (m, 4H), 1.58 (m, 8H), 1.29 (m, 24H), 1.12 (m, 20H), 0.86 (m, 12H), 0.79 (m, 10H). ¹³C NMR (75 MHz, Chloroform-*d*) δ 181.84,

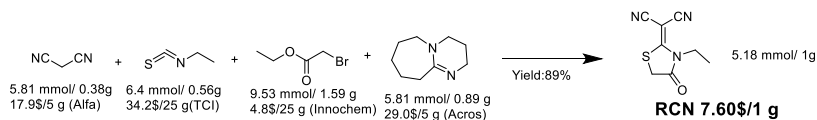
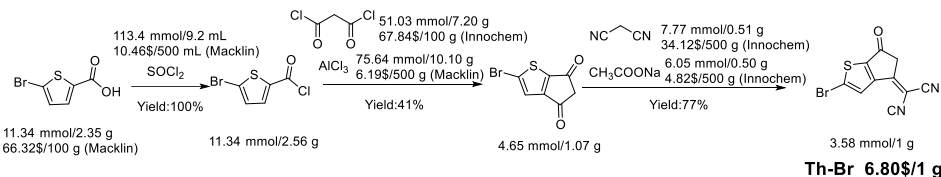
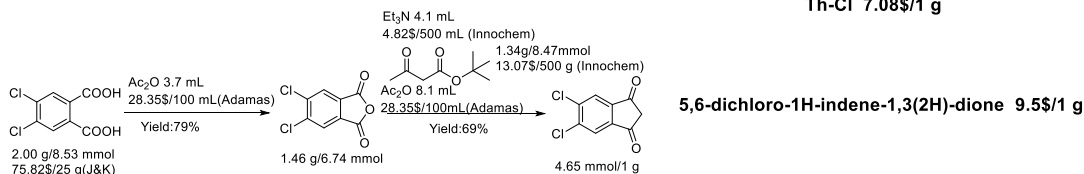
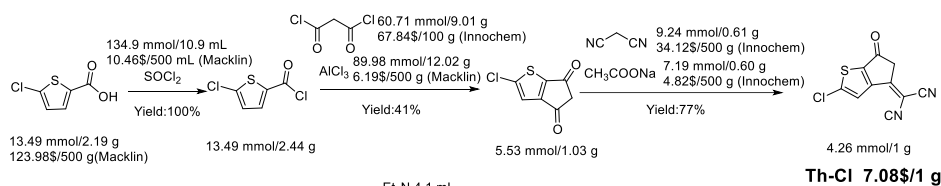
180.22, 159.20, 157.47, 155.23, 152.72, 142.21, 142.03, 140.88, 139.55, 138.98, 136.81, 135.74, 128.64, 127.84, 122.75, 118.39, 116.30, 113.63, 69.40, 67.15, 62.89, 54.70, 40.38, 35.58, 31.80, 31.72, 31.30, 30.05, 29.27, 29.23, 29.16, 24.16, 22.63, 22.61, 14.11. MS (MALDI-TOF): m/z Calcd. for $C_{109}H_{112}Cl_2N_4O_2S_4$: 1707.71 [M], Found 1707.92 [M]⁺.

FPCC-Br:

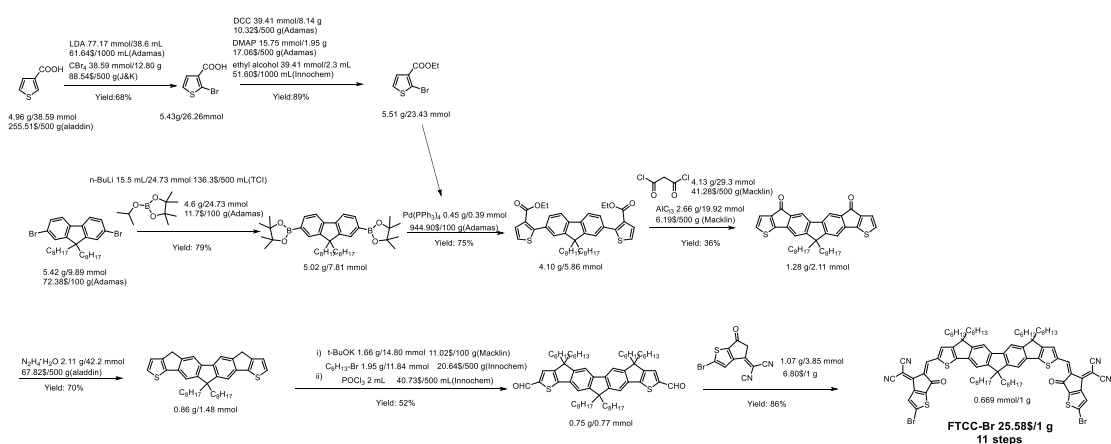


In a 50 mL of two-neck round bottom flask, compound 5 (200mg, 0.157 mmol) and Th-Br (218.8 mg, 0.784 mmol) were dissolved in 5 mL of $CHCl_3$, and then 0.20 mL of pyridine was added into the mixture by syringe. The reaction was stirred at room temperature overnight. The solvent was removed under vacuum and the residue was purified by silica gel column using $CHCl_3$ as eluent. The product FPCC-Br was obtained as blue black solid (231.5 mg, 82%). ¹H NMR (400 MHz, Chloroform-*d*) δ 8.63 (s, 1H), 8.60 (s, 1H), 7.98 (s, 1H), 7.66 – 7.61 (m, 4H), 7.59 (s, 2H), 7.42 (s, 1H), 7.10 (q, $J = 8.2$ Hz, 16H), 2.55 (t, $J = 7.9$ Hz, 8H), 2.11 – 2.01 (m, 4H), 1.58 (m, 8H), 1.29 (s, 24H), 1.12 (s, 20H), 0.86 (t, $J = 6.7$ Hz, 12H), 0.79 (m, 10H). ¹³C NMR (75 MHz, Chloroform-*d*) δ 181.43, 179.80, 159.24, 157.48, 152.73, 151.09, 142.22, 142.03, 140.88, 139.60, 139.00, 137.06, 135.75, 128.65, 127.85, 126.08, 122.42, 118.40, 116.33, 113.87, 62.89, 54.71, 40.38, 35.58, 31.80, 31.73, 31.34, 31.30, 30.06, 29.27, 29.24, 29.16, 24.17, 22.64, 22.61, 14.15, 14.12. MS (MALDI-TOF): m/z Calcd. for $C_{109}H_{112}Br_2N_4O_2S_4$: 1797.60 [M], Found 1797.75 [M]⁺.

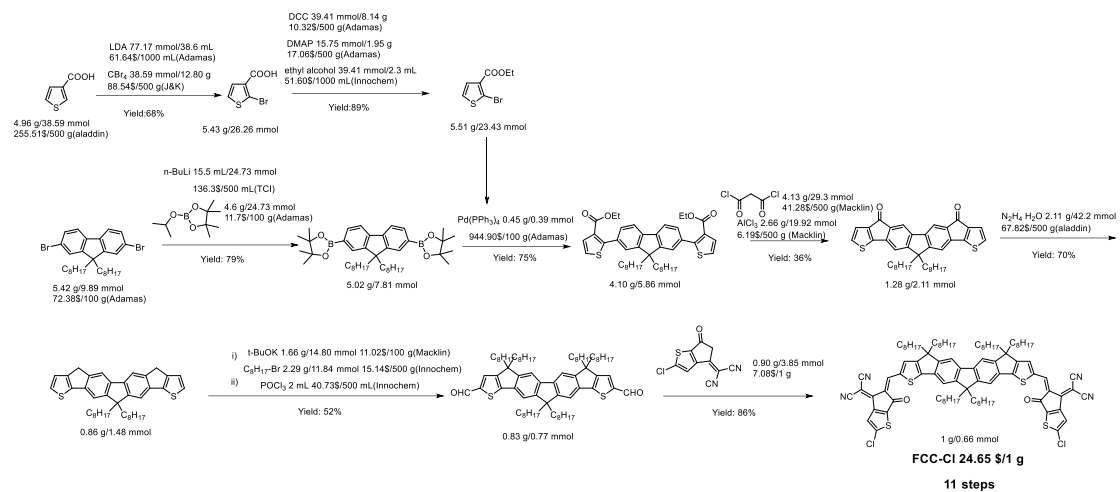
The calculation of material-only cost



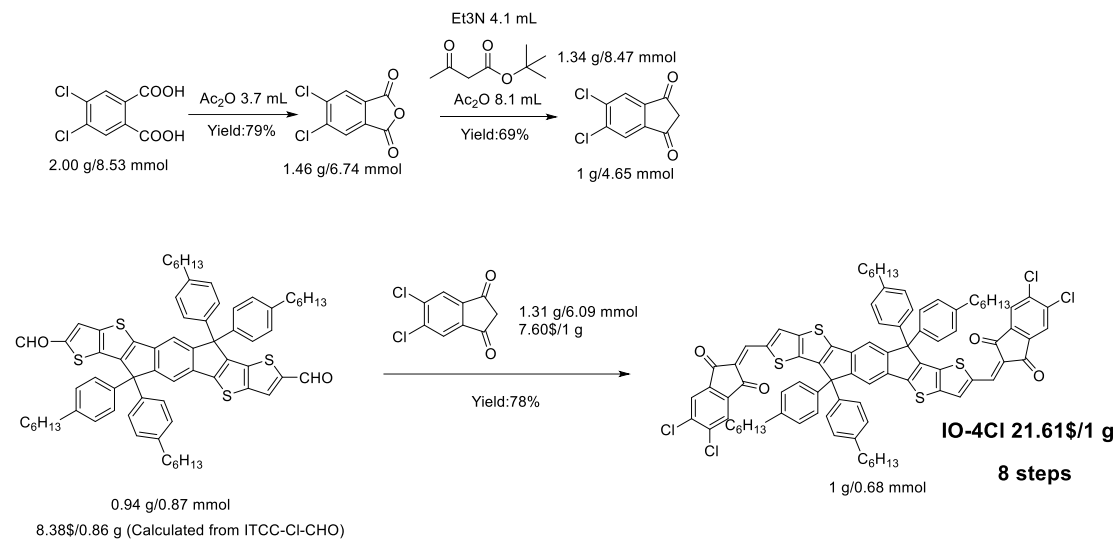
The synthetic route of end groups.



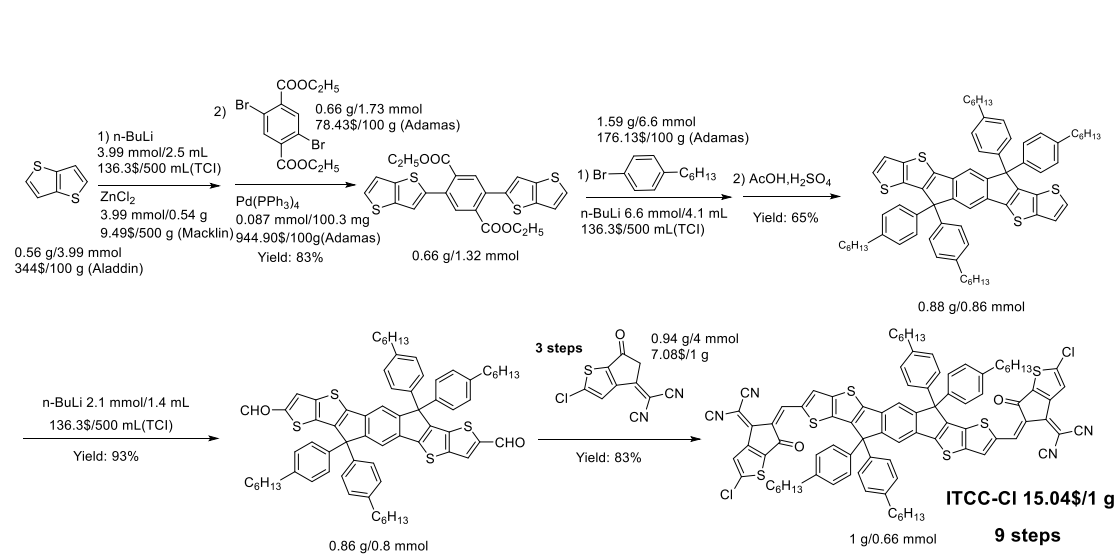
The synthetic route of FTCC-Br.



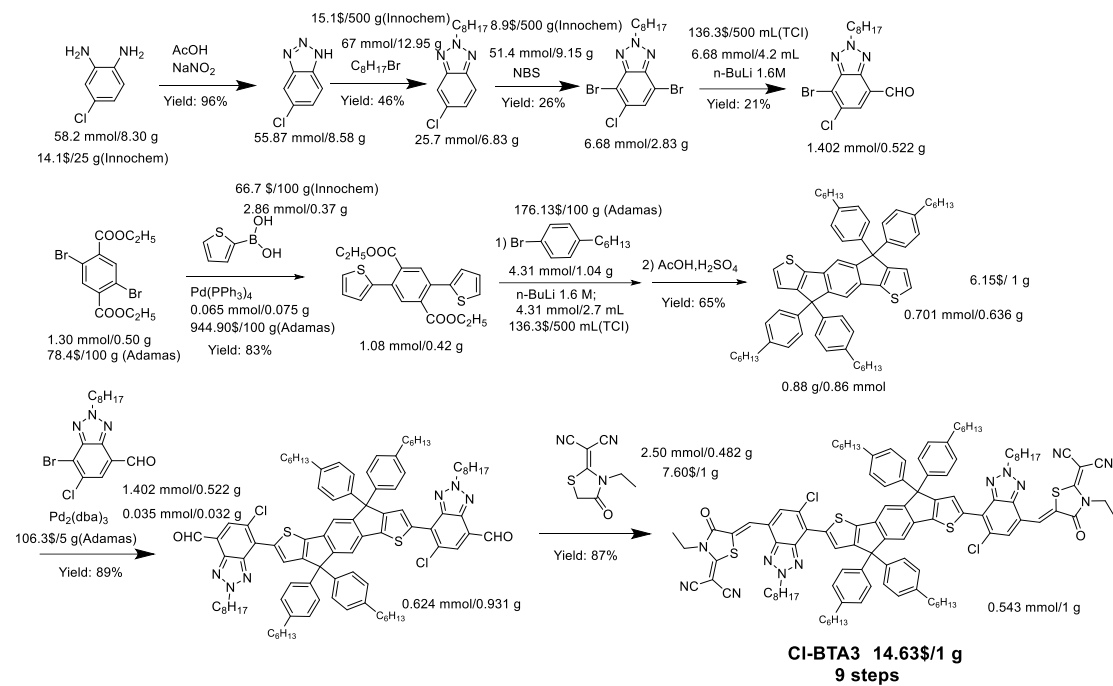
The synthetic route of FCC-Cl.



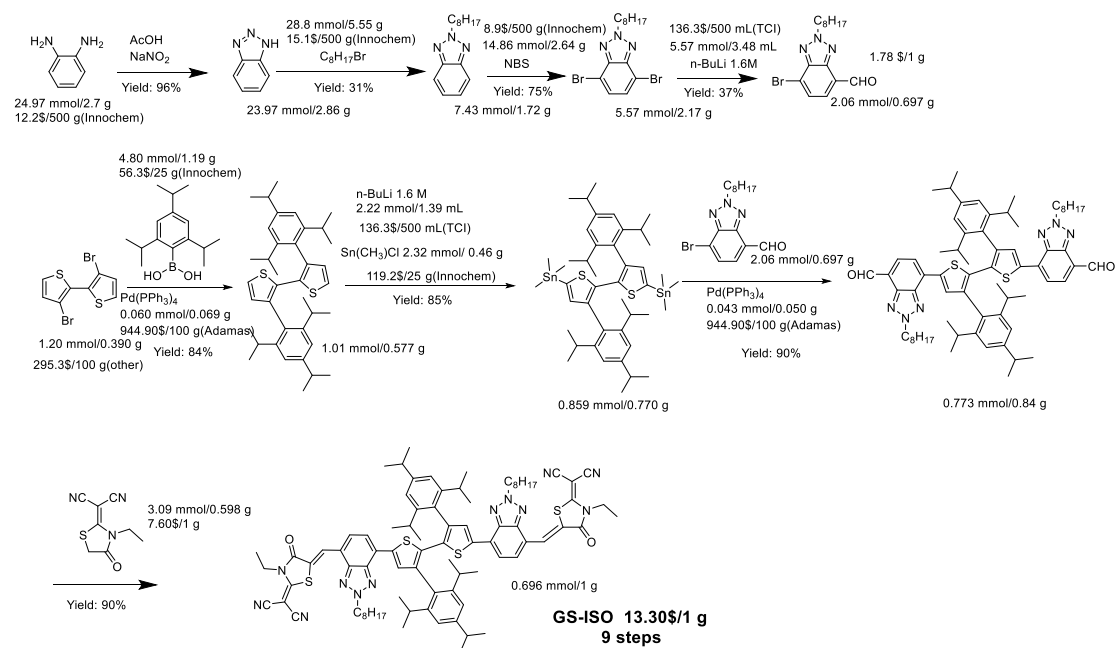
The synthetic route of IO-4Cl.



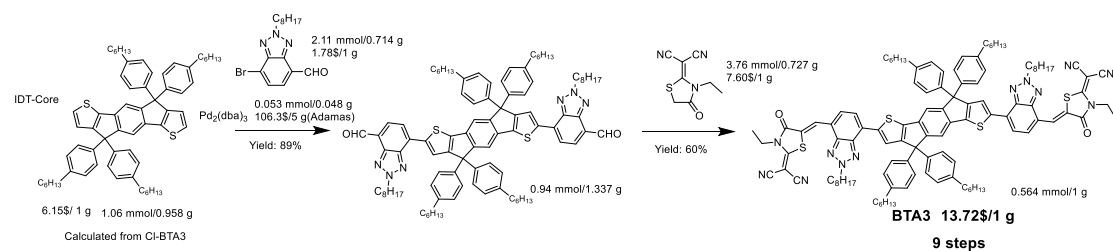
The synthetic route of ITCC-Cl.



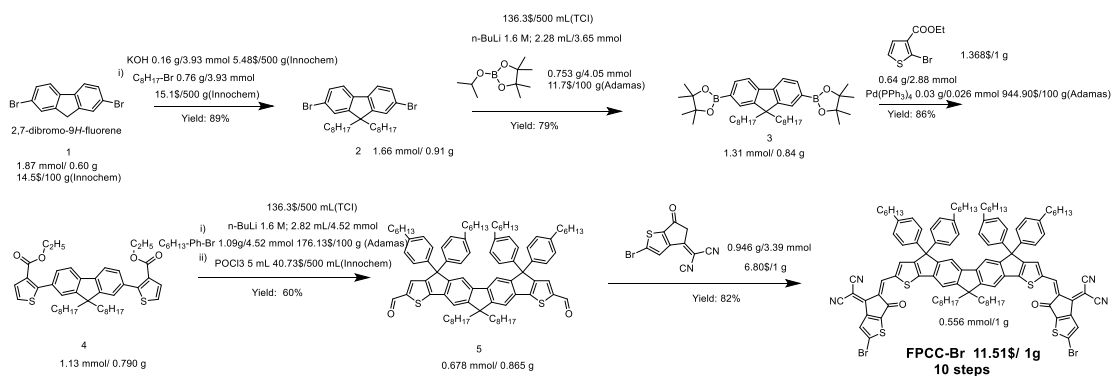
The synthetic route of Cl-BTA3.



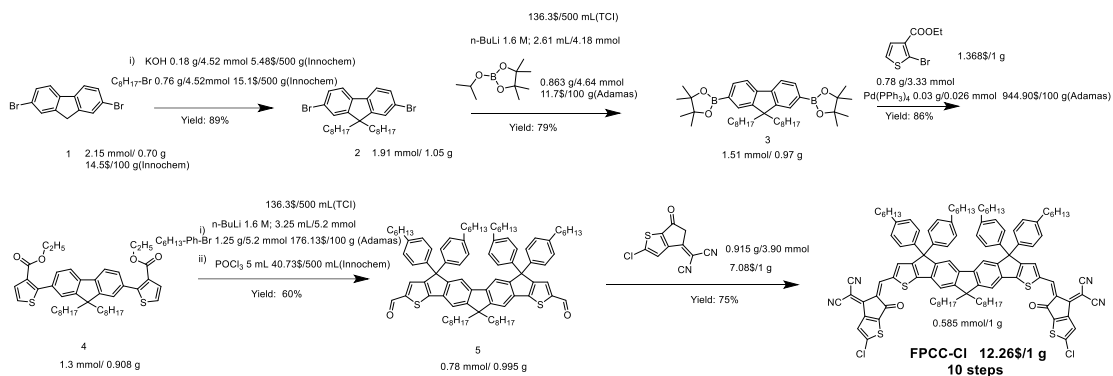
The synthetic route of GS-ISO.



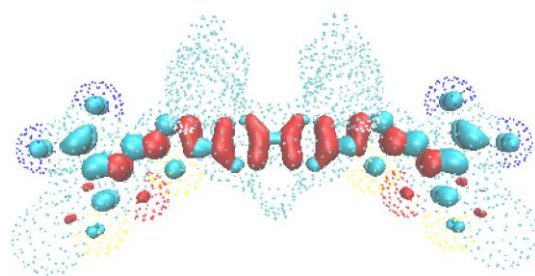
The synthetic route of Cl-BTA3.



The synthetic route of FPCC-Br.



The synthetic route of FPCC-Cl.



FPCC-Cl = 0.0080 a.u.

Figure S1. The overlap and the exchange integrals of HOMO (red) and LUMO (sky blue) distributions of FPCC-Cl.

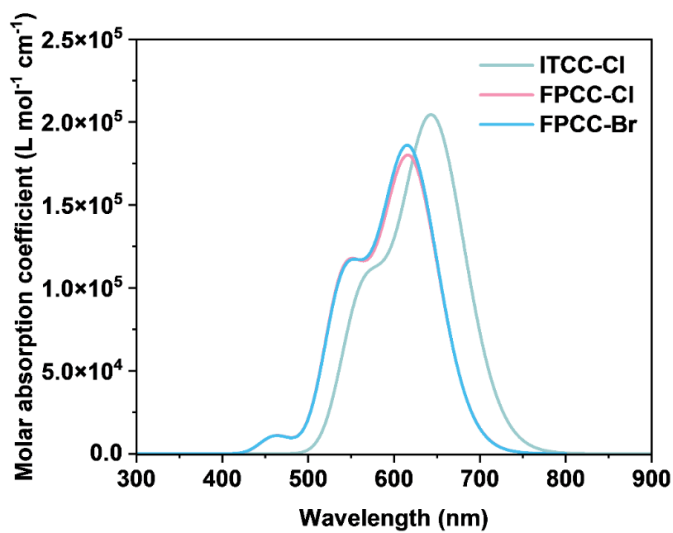


Figure S2. The calculated molar absorption coefficient of ITCC-Cl, FPCC-Cl, and FPCC-Br.

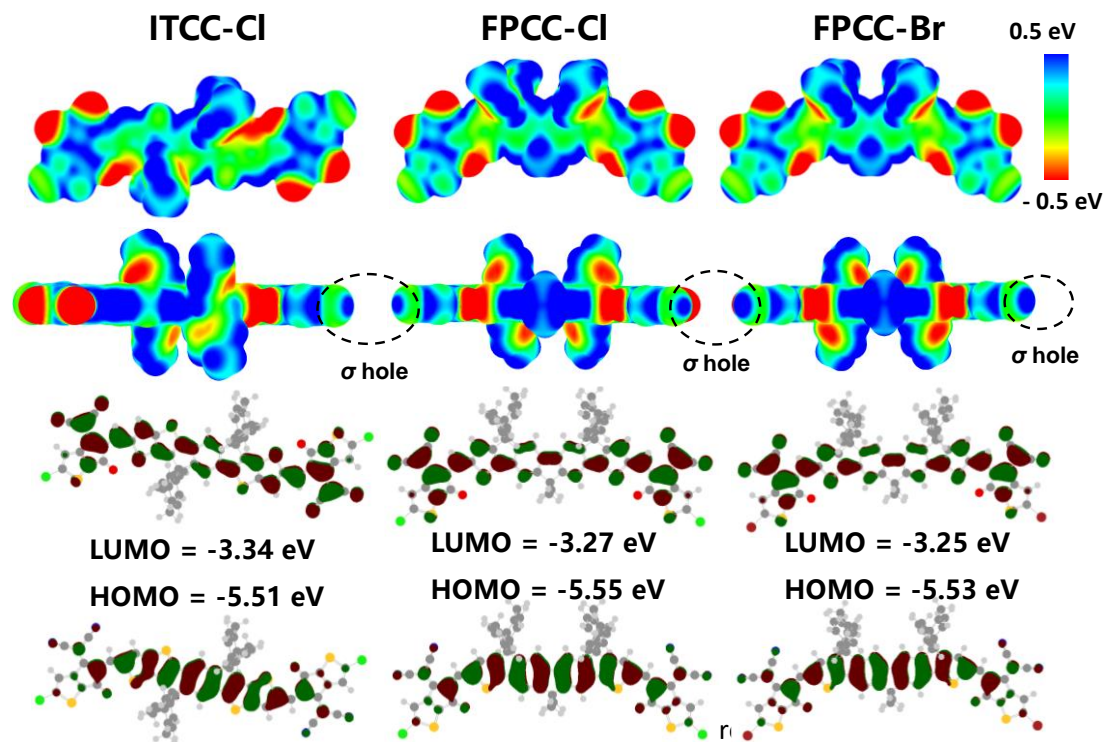


Figure S3. The calculated ESP, LUMO and HOMO levels of ITCC-Cl, FPCC-Cl, and FPCC-Br.

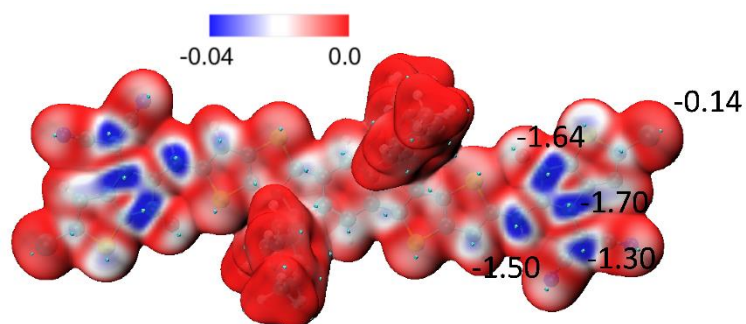


Figure S4. The calculated local electron attachment energy of ITCC-Cl.

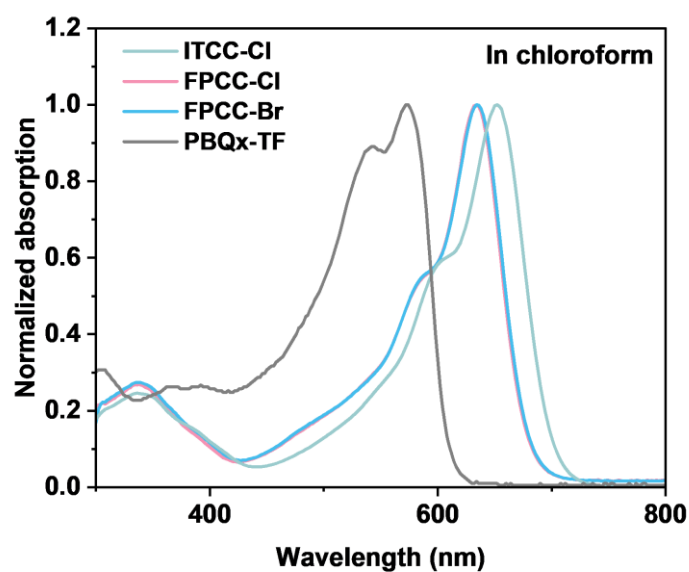


Figure S5. The UV-Vis absorption spectroscopy in chloroform of ITCC-Cl, FPCC-Cl, FPCC-Br, and PBQx-TF.

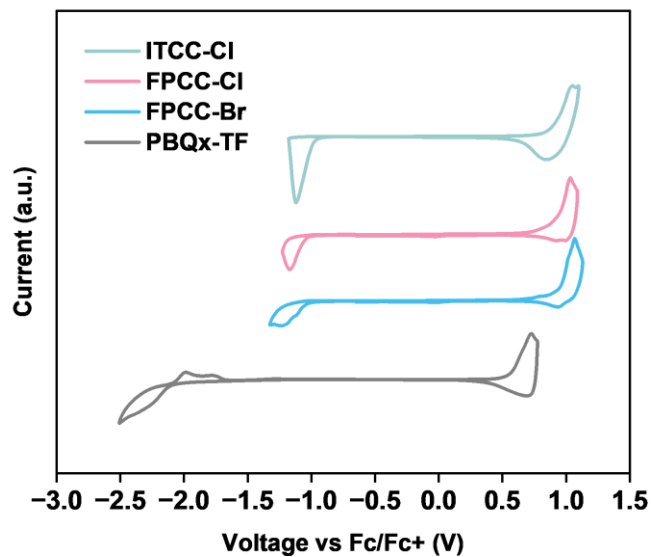


Figure S6. The electrochemical curves of ITCC-Cl, FPCC-Cl, FPCC-Br, and PBQx-TF measured by cyclic voltammetry.

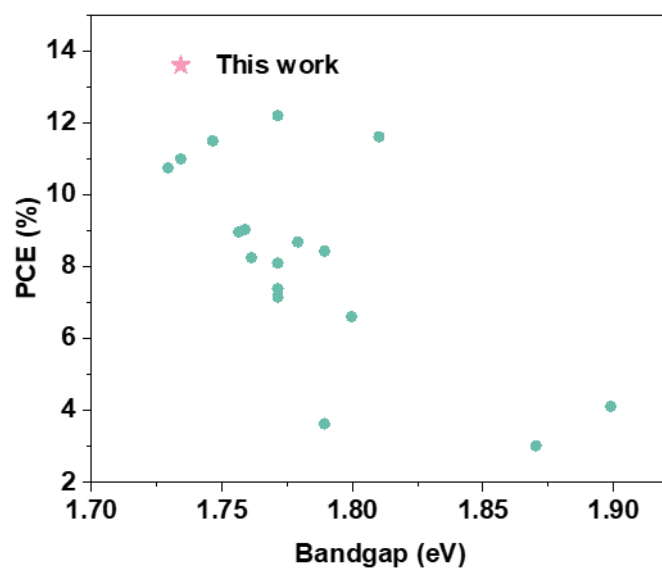


Figure S7. The PCE statistics of the reported WBG acceptor-based OPV cells with bandgap above 1.72 eV.

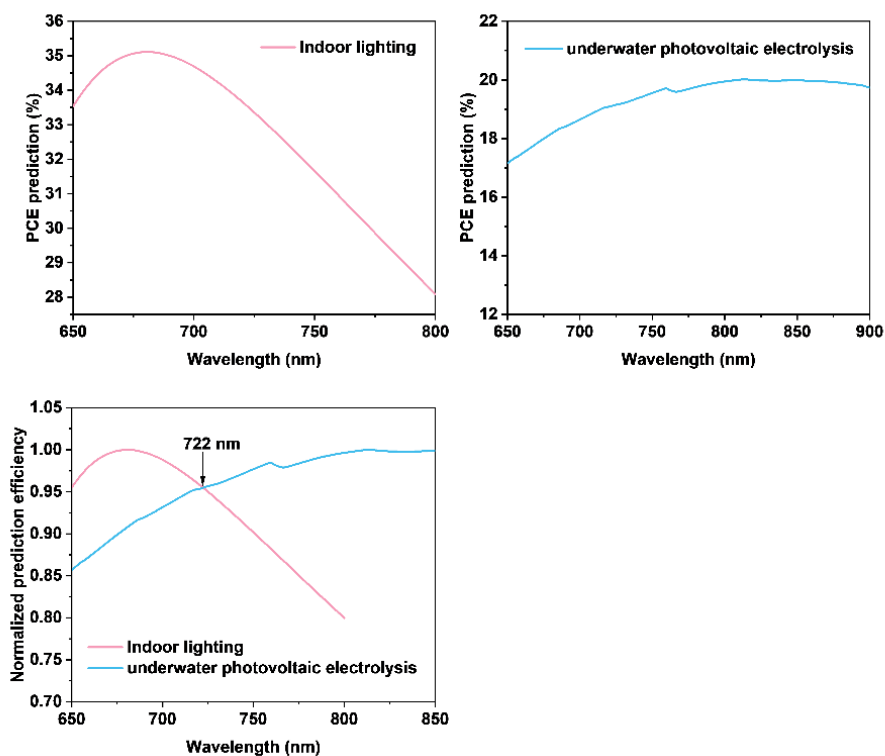


Figure S8. The theoretical PCE of OPV materials with different bandgaps under indoor light conditions at 1000 lux and underwater at a depth of 5cm.

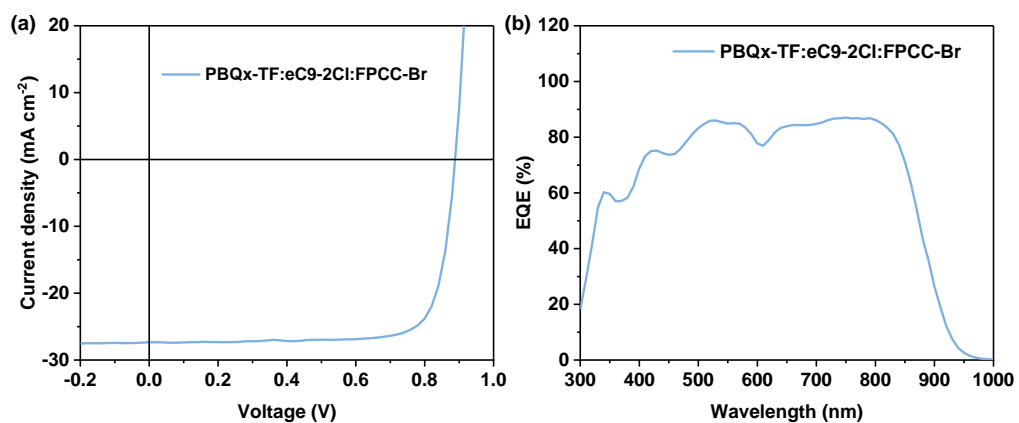


Figure S9. The J-V and EQE curves of the ternary cell based PBQx-TF:eC9-2Cl:FPCC-Br (D:A ratio = 1:1:0.2).

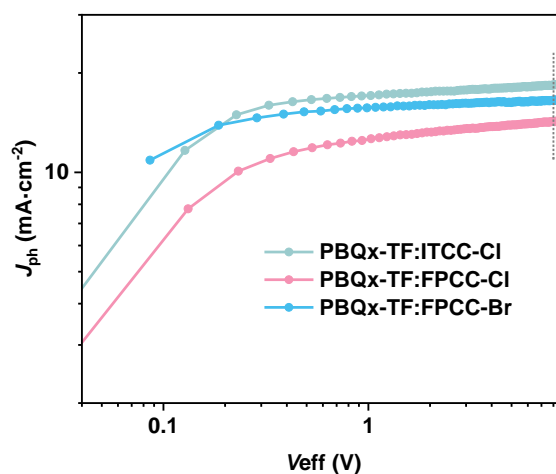


Figure S10. The exciton dissociation efficiency of ITCC-Cl, FPCC-Cl, FPCC-Br, and PBQx-TF measured by cyclic voltammetry.

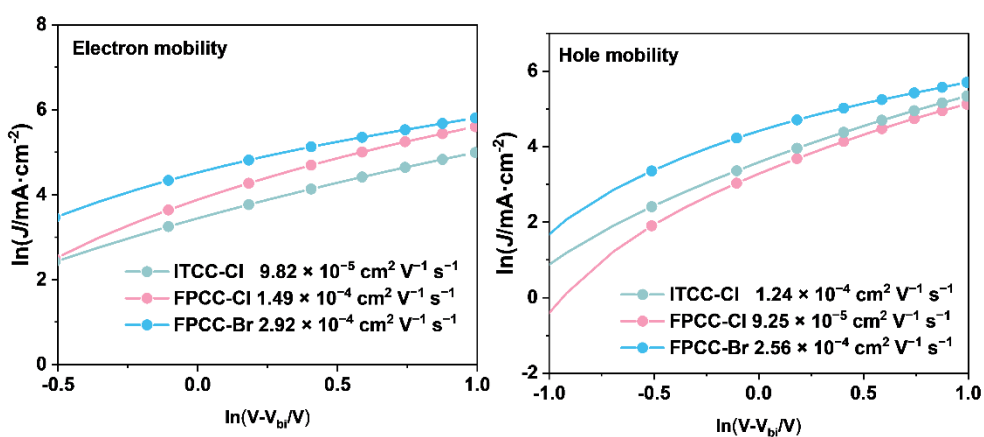


Figure S11. The electron and hole mobility of the blend film.

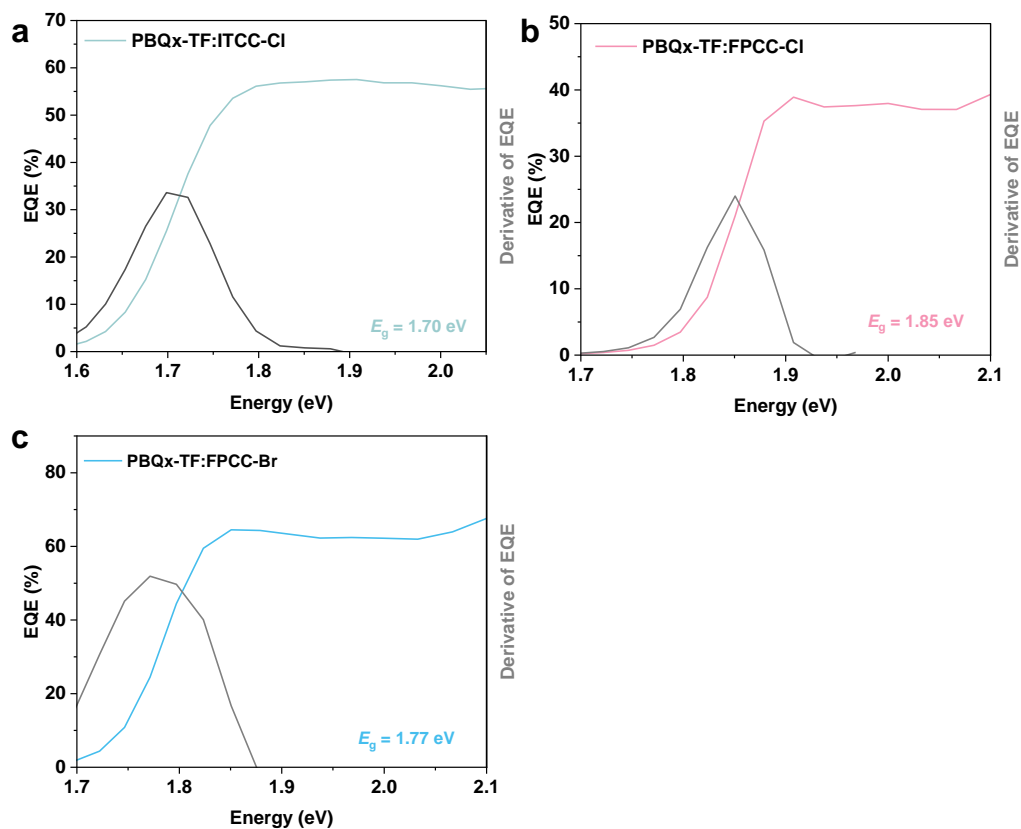


Figure S12. The derivative of high-sensitive EQE of (a) PBQx-TF:ITCC-Cl-, (b) PBQx-TF:FPCC-Cl-, and (c) PBQx-TF:FPCC-Br-based devices.

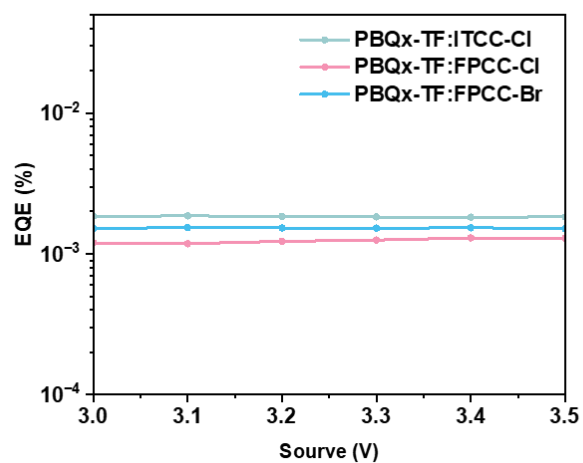


Figure S13. The E_{EQE} curves of PBQx-TF:ITCC-Cl-, PBQx-TF:FPCC-Cl-, and PBQx-TF:FPCC-Br-based devices.

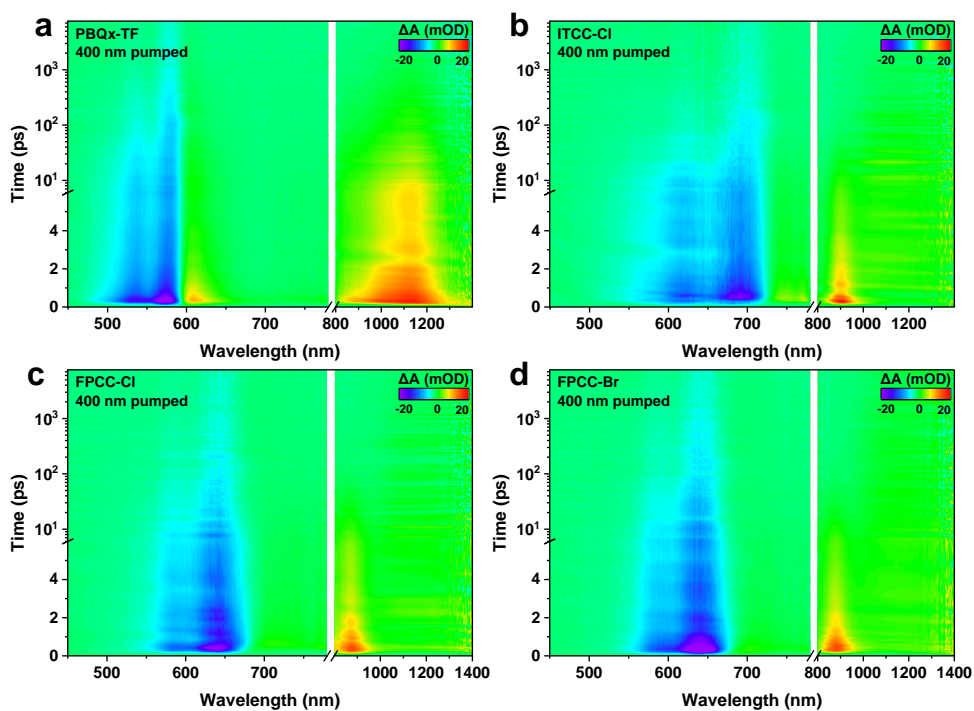


Figure S14. 2D TA spectroscopy for PBQx-TF-, ITCC-Cl-, FPCC-Cl-, and FPCC-Br-based neat films.

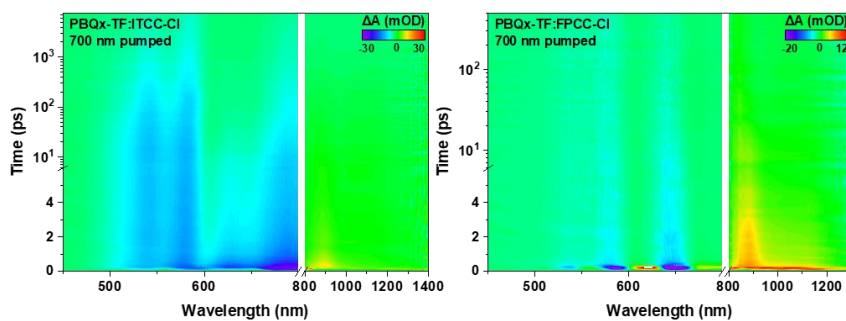


Figure S15. Two-dimensional TA spectroscopy for PBQx-TF:ITCC-Cl- and PBQx-TF:FPCC-Cl-based blend films.

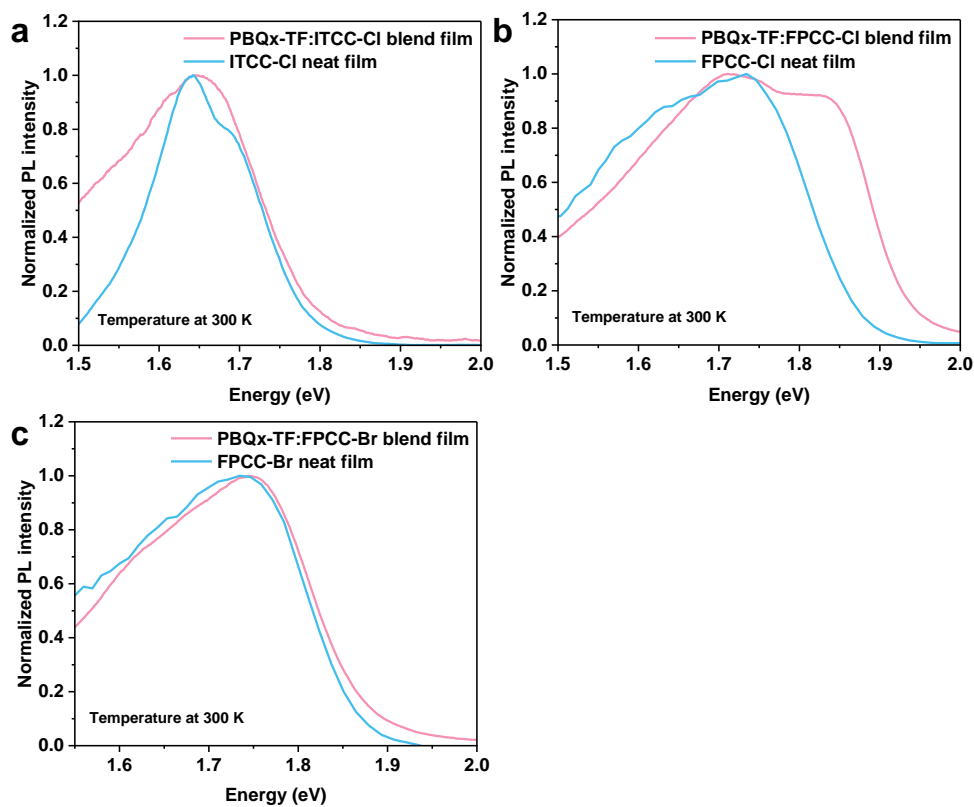


Figure S16. The PL spectra of ITCC-Cl-, FPCC-Cl-, and FPCC-Br-based blend and neat films.

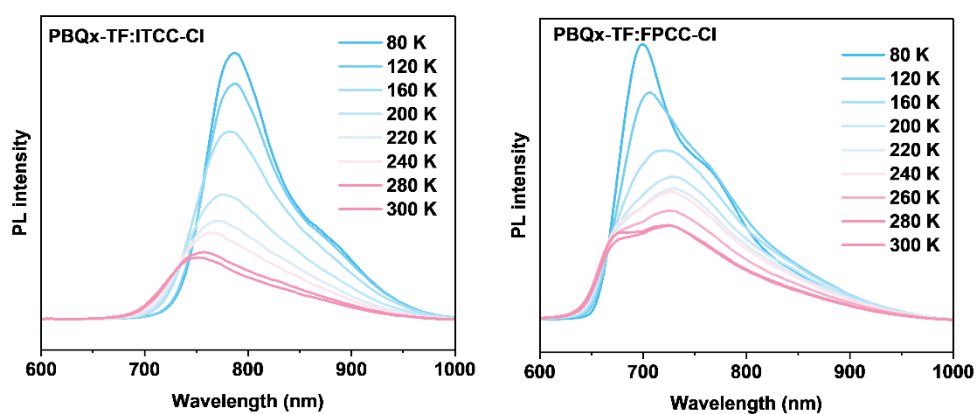


Figure S17. The TD-PL spectra of ITCC-Cl- and FPCC-C--based neat films.

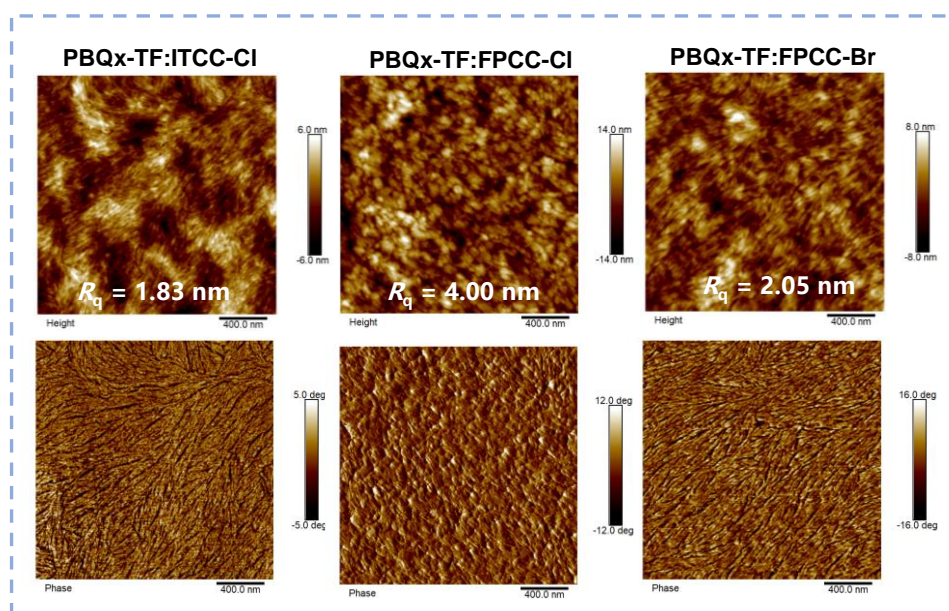


Figure S18. The AFM height and phase images of ITCC-Cl-, FPCC-Cl-, and FPCC-Br-based blend films.

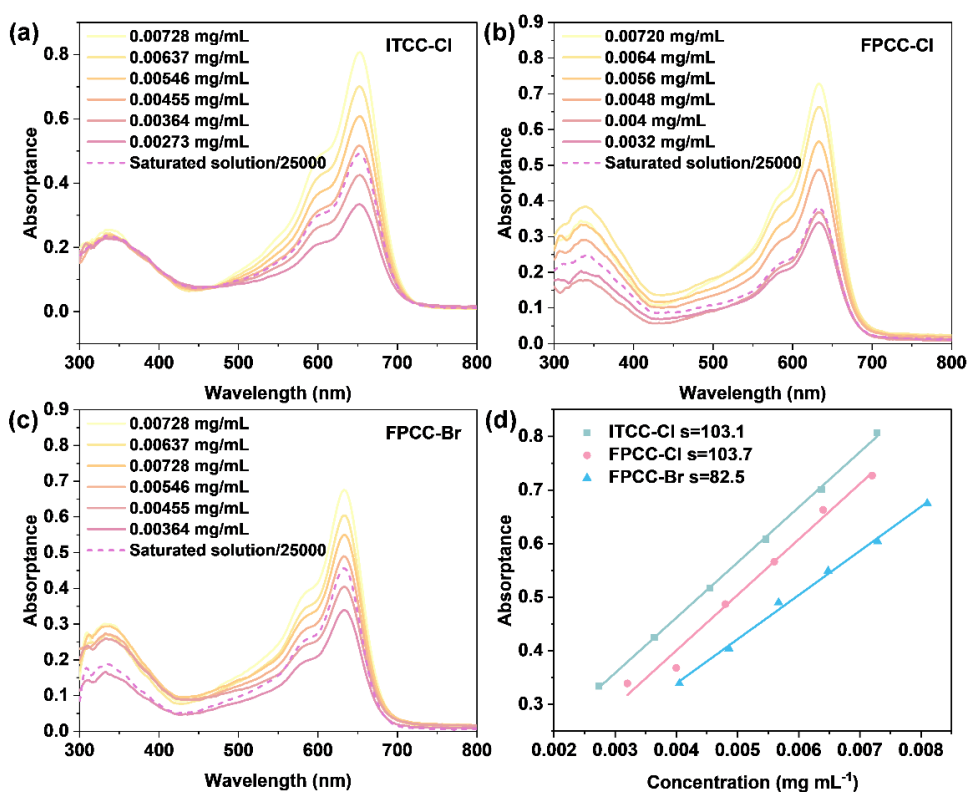


Figure S19. The UV absorption spectra of different concentrations and standard curves three of acceptors.

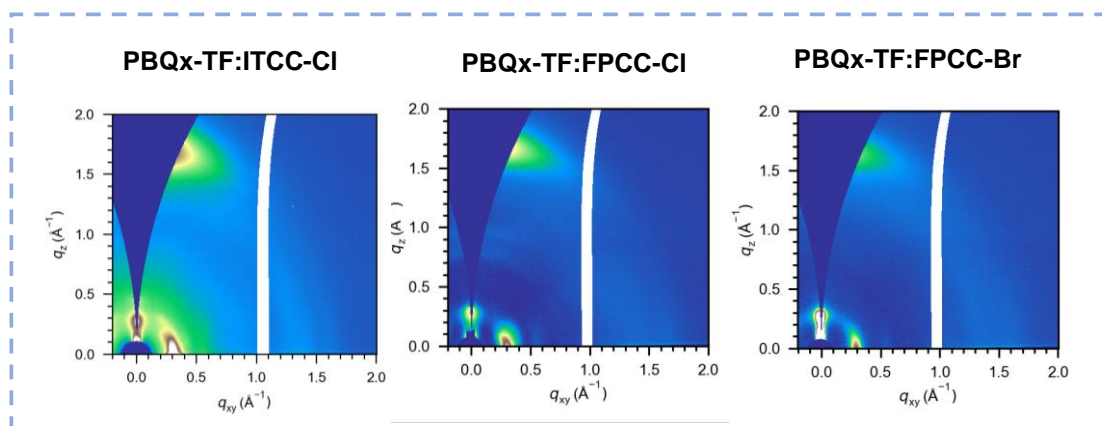


Figure S20. The 2D GIWAXS patterns of ITCC-Cl-, FPCC-Cl-, and FPCC-Br-based blend films.

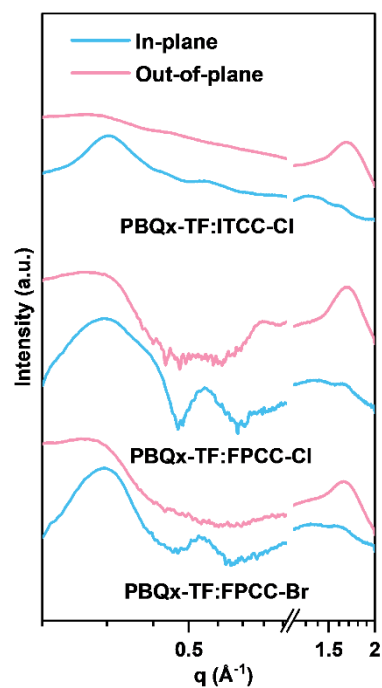


Figure S21. The 1D line-cut profiles in IP and OOP directions of ITCC-Cl-, FPCC-Cl-, and FPCC-Br-based devices.

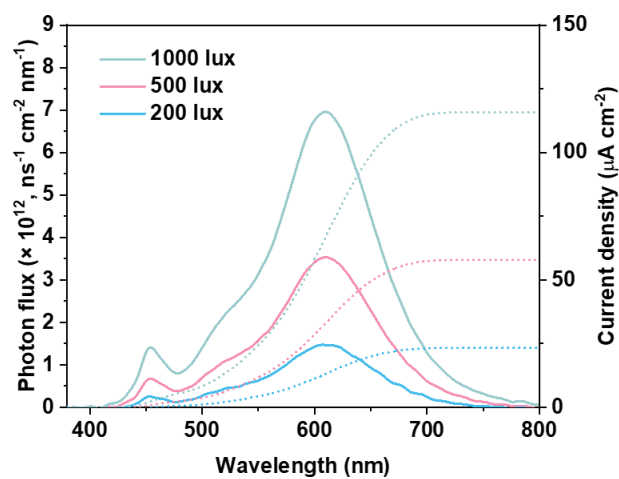


Figure S22. The photon flux and integral current density for PBQx-TF:FPCC-Br-based device of 2700 K LED lamp under different light intensities.

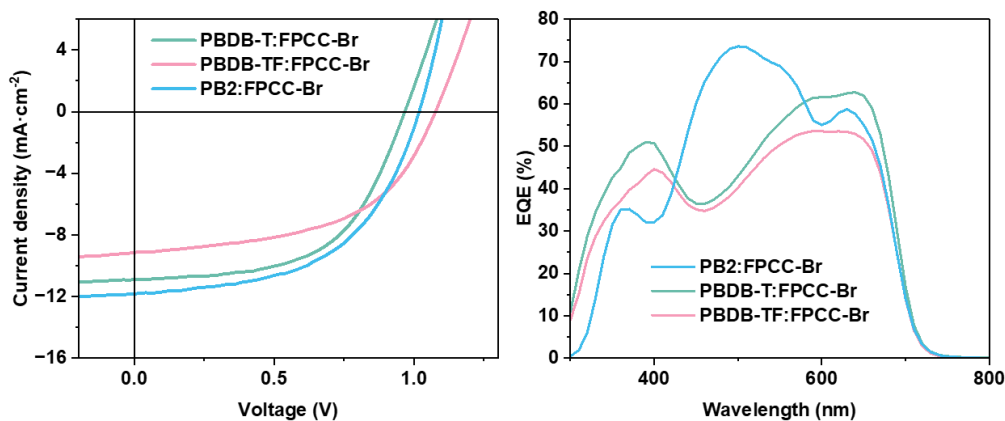


Figure S23. The $J-V$ and EQE curves of PBDB-T:FPCC-Br-, PBDB-TF:FPCC-Br-, and PB2:FPCC-Br-based devices under AM 1.5G irradiation. (with the effective devices area of 0.39 cm^2 for indoor OPV application).

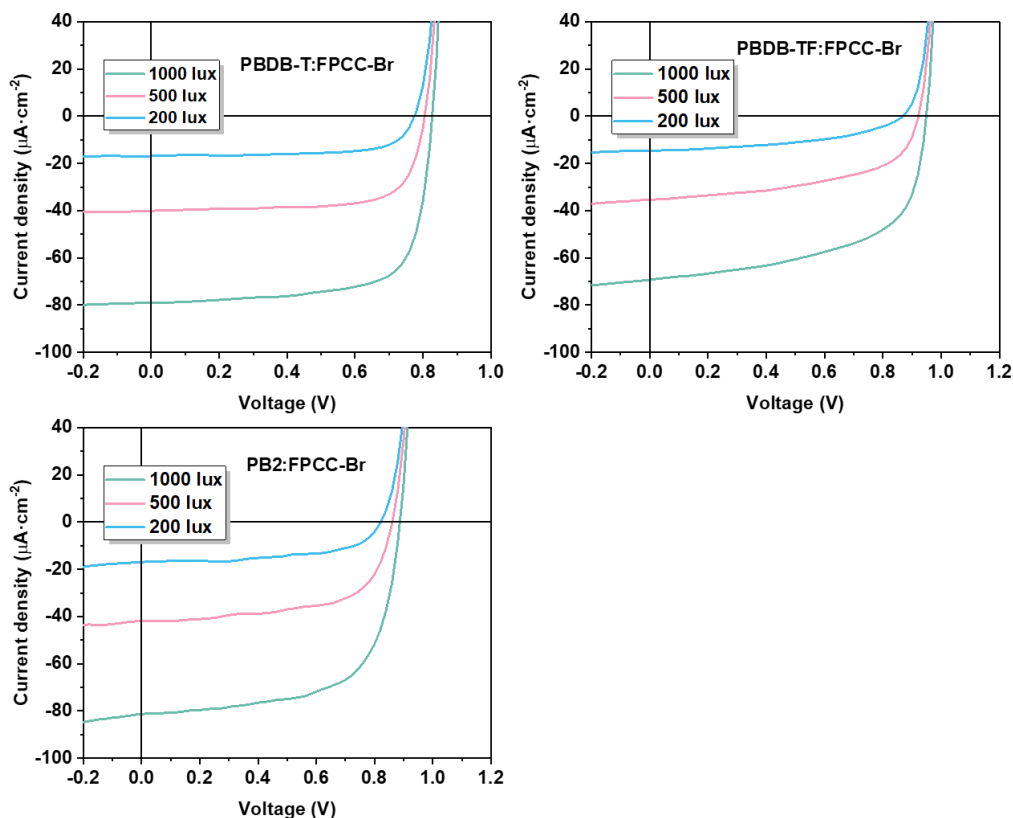


Figure S24. The $J-V$ curves of PBDB-T:FPCC-Br-, PBDB-TF:FPCC-Br-, and PB2:FPCC-Br-based devices under indoor light irradiation. (with the effective devices area of 0.39 cm^2 for indoor OPV application).

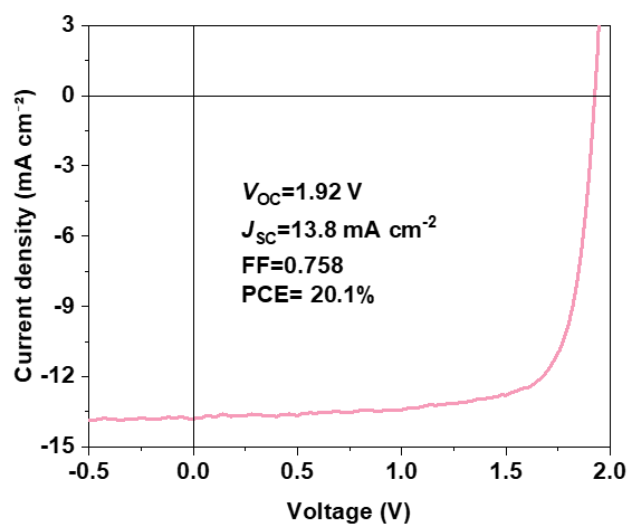


Figure S25. The J - V curves of the tandem cell based on PBQx-TF:FPCC-Br as front cell and PBDB-TF:BTP-eC9:HDO-4Cl as rear cell.

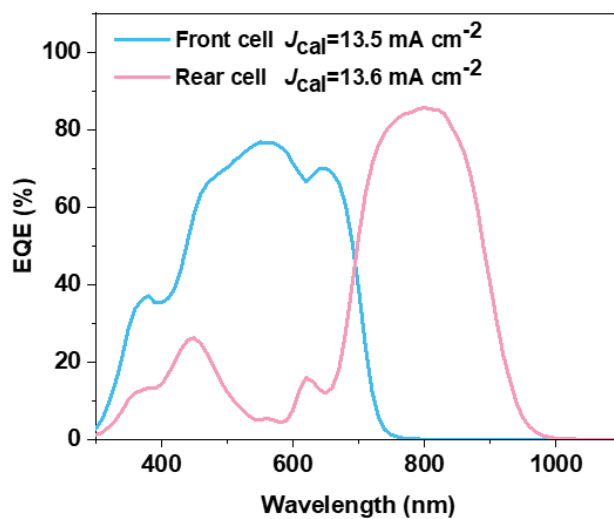


Figure S26. The EQE curves of the tandem cell based on PBQx-TF:FPCC-Br as the front cell and PBDB-TF:BTP-eC9:HDO-4Cl as the rear cell.

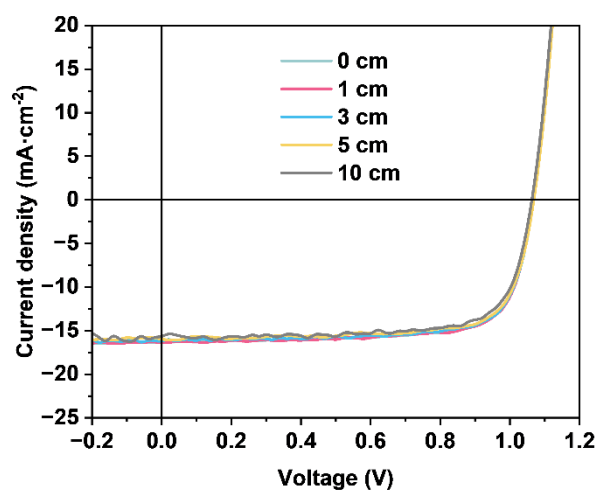


Figure S27. The J - V curves at different depths underwater under the AM 1.5G illumination of FPCC-Br-based blend films.

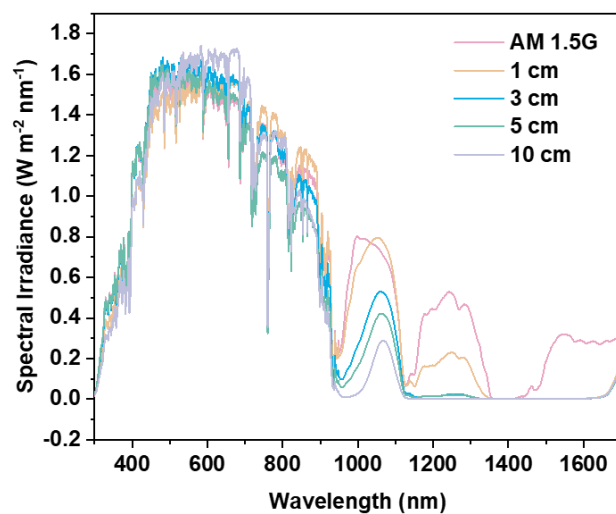


Figure S28. The actual AM 1.5G spectral irradiance and the spectral irradiance at different water depths.

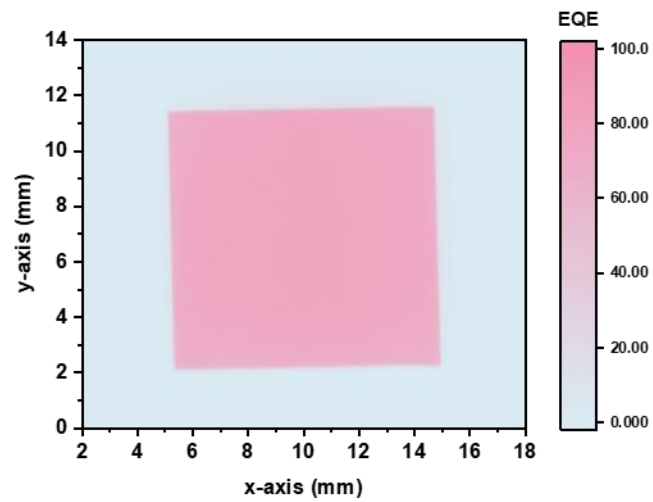


Figure S29. The EQE mapping of 1 cm² FPCC-Br-based cell.

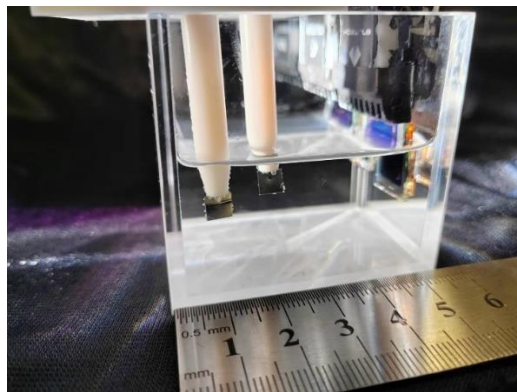


Figure S30. The physical diagram of two series connected batteries directly used for underwater photovoltaic electrolysis.

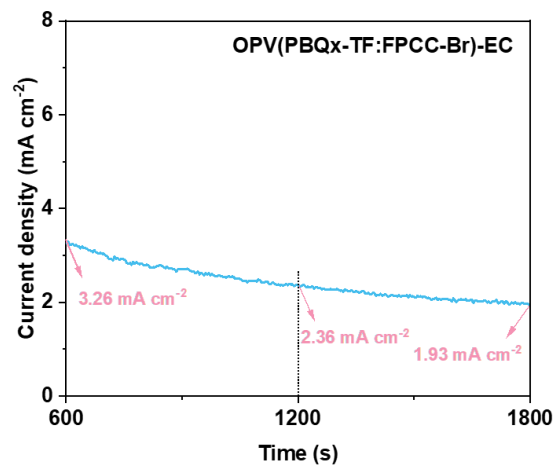


Figure S31. The chronoamperometric measurement of two FPCC-Br-based cells connected in series.

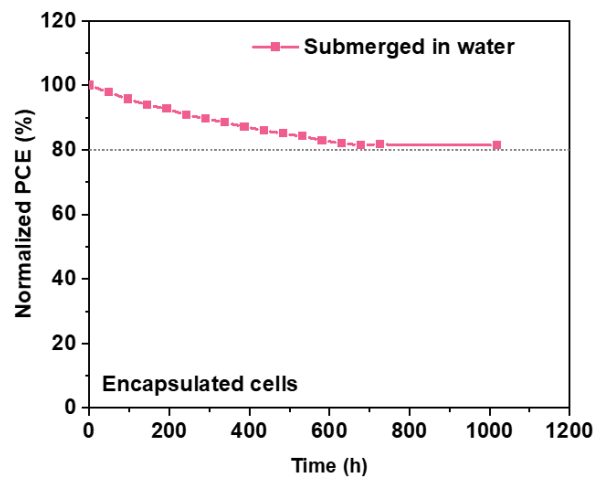


Figure S32. The underwater stability measurement of FPCC-Br-based cells.

Table S1. The PCE statistics of the reported WBG acceptor-based OPV cells with bandgap below 720 nm.

Donors	Acceptors	Absorption edges (nm)	Bandgaps (eV)	Power conversion efficiency (%)	References
J52-F	BTA3	705	1.76	9.04	Ref. ^[3]
PBQx-TF	F-BTA3	710	1.75	11.5	Ref. ^[4]
PBQx-TC1	BTA3	700	1.77	12.2	Ref. ^[5]
J61	BTA1	663	1.87	3.02	Ref. ^[6]
J61	BTA3	704	1.76	8.25	Ref. ^[6]
PE25	Cl-BTA3	717	1.73	10.75	Ref. ^[7]
PB2	ITCC	715	1.73	11.0	Ref. ^[8]
PBDB-TF	GS-ISO	685	1.81	11.62	Ref. ^[9]
PBDB-TF	GS-OC6	697	1.78	8.69	Ref. ^[9]
PBDB-TF	GS-OEH	693	1.79	8.44	Ref. ^[9]
PDBT-T1	SdiPBI-S	700	1.77	7.16	Ref. ^[10]
PDBT-T1	IC-1IDT-IC	700	1.77	7.39	Ref. ^[11]
PSEHTT	DBFI-EDOT	700	1.77	8.1	Ref. ^[12]
P3HT	F4TBT4	653	1.90	4.12	Ref. ^[13]
PDBT-T1	SdiPBI-BT	689	1.80	6.61	Ref. ^[14]
PBQx-TF	ITCC-Cl	744	1.67	12.3	This work
PBQx-TF	FPCC-Cl	706	1.76	8.96	This work
PBQx-TF	FPCC-Br	715	1.73	13.6	This work

Table S2. Photovoltaic parameters of the PBQx-TF:eC9-2Cl:FPCC-Br -based cells.

Blends	V_{oc} (V)	J_{sc} (mA cm ⁻²)	J_{cal} (mA cm ⁻²)	FF	PCE (%)
PBQx-TF:eC9-2Cl:FPCC-Br	0.888	27.3	26.7	0.796	19.3 (19.1±0.1)

Table S3. The voltage loss analysis of ITCC-Cl-, FPCC-Cl-, and FPCC-Br-based devices.

blends	E_g (eV)	V_{oc} (V)	V_{loss} (V)	ΔV_1 (V)	ΔV_2 (V)	ΔV_3 (V)
PBQx-TF:ITCC-Cl	1.70	0.984	0.716	0.282	0.141	0.293
PBQx-TF:FPCC-Cl	1.85	1.080	0.770	0.292	0.190	0.288
PBQx-TF:FPCC-Br	1.77	1.070	0.700	0.286	0.130	0.284

Table S4. The parameters obtained from GIWAXS measurements.

	q_z (\AA^{-1})	π - π distance (\AA)	FWHM (\AA^{-1})	CCL (\AA)	q_{xy} (\AA^{-1})	Lamellar distance (\AA)
PBQx-TF:ITCC-Cl	1.675	3.75	0.223	25.4	0.305	20.6
PBQx-TF:FPCC-Cl	1.675	3.75	0.216	26.2	0.295	21.3
PBQx-TF:FPCC-Br	1.648	3.81	0.188	30.1	0.295	21.3

Table S5. Photovoltaic parameters of the PBQx-TF:FPCC-Br-based cells under the 2700 K LED lamp with different light intensities.

Light intensities [lux]	P_{in} [$\mu\text{W cm}^{-2}$]	V_{oc} [V]	J_{sc} [$\mu\text{A cm}^{-2}$]	J_{cal}^a [$\mu\text{A cm}^{-2}$]	FF	P_{out} [$\mu\text{W cm}^{-2}$]	PCE ^b [%]
200 lux	59.9	0.863	24.4	23.3	0.740	15.6	26.0 (25.9 \pm 0.1)
500 lux	152	0.896	59.8	57.8	0.763	40.9	26.9 (26.8 \pm 0.1)
1000 lux	306	0.940	122	116	0.780	89.5	29.3 (29.1 \pm 0.2)

^{a)} The calculated current density from corresponding EQE spectra; ^{b)} The average PCEs obtained from 5 independent devices.

Table S6. Photovoltaic parameters of the PBDB-T:FPCC-Br-, PBDB-TF:FPCC-Br-, and PB2:FPCC-Br-based cells under AM 1.5G irradiation.

Blends	V_{oc} [V]	J_{sc} [$\mu\text{A cm}^{-2}$]	J_{cal}^a [$\mu\text{A cm}^{-2}$]	FF	PCE ^b [%]
PBDB-T:FPCC-Br	0.967	10.9	10.4	0.564	5.94 (5.88 \pm 0.07)
PBDB-TF:FPCC-Br	1.08	9.14	9.18	0.528	5.21 (5.10 \pm 0.08)
PB2:FPCC-Br	1.02	11.8	11.5	0.533	6.41 (6.34 \pm 0.07)

^{a)} The calculated current density from corresponding EQE spectra; ^{b)} The average PCEs obtained from 5 independent devices.

Table S7. Photovoltaic parameters of the PBDB-T:FPCC-Br-based cells under the 2700 K LED lamp with different light intensities.

Light intensities [lux]	P_{in} [$\mu\text{W cm}^{-2}$]	V_{oc} [V]	J_{sc} [$\mu\text{A cm}^{-2}$]	J_{cal}^a [$\mu\text{A cm}^{-2}$]	FF	P_{out} [$\mu\text{W cm}^{-2}$]	PCE ^b [%]
200 lux	59.9	0.774	16.8	15.9	0.692	9.03	15.1 (14.9 \pm 0.2)
500 lux	152	0.805	40.0	39.3	0.724	23.3	15.3 (15.3 \pm 0.1)
1000 lux	306	0.827	78.9	78.6	0.724	47.3	15.5 (15.4 \pm 0.1)

a) The calculated current density from corresponding EQE spectra; b) The average PCEs obtained from 5 independent devices.

Table S8. Photovoltaic parameters of the PBDB-TF:FPCC-Br-based cells under the 2700 K LED lamp with different light intensities.

Light intensities [lux]	P_{in} [$\mu\text{W cm}^{-2}$]	V_{oc} [V]	J_{sc} [$\mu\text{A cm}^{-2}$]	J_{cal}^a [$\mu\text{A cm}^{-2}$]	FF	P_{out} [$\mu\text{W cm}^{-2}$]	PCE ^b [%]
200 lux	59.9	0.867	14.7	13.9	0.459	5.83	9.73 (9.53 \pm 0.14)
500 lux	152	0.922	35.4	34.3	0.535	17.5	11.5 (11.2 \pm 0.3)
1000 lux	306	0.949	69.2	68.5	0.588	38.6	12.6 (12.5 \pm 0.1)

a) The calculated current density from corresponding EQE spectra; b) The average PCEs obtained from 5 independent devices.

Table S9. Photovoltaic parameters of the PB2:FPCC-Br-based cells under the 2700 K LED lamp with different light intensities.

Light intensities [lux]	P_{in} [$\mu\text{W cm}^{-2}$]	V_{oc} [V]	J_{sc} [$\mu\text{A cm}^{-2}$]	J_{cal}^a [$\mu\text{A cm}^{-2}$]	FF	P_{out} [$\mu\text{W cm}^{-2}$]	PCE ^b [%]
200 lux	59.9	0.822	16.9	16.5	0.587	8.14	13.6 (13.5 \pm 0.1)
500 lux	152	0.861	41.7	40.8	0.629	22.6	14.9 (14.6 \pm 0.2)
1000 lux	306	0.887	81.3	81.7	0.650	46.9	15.3 (15.1 \pm 0.1)

a) The calculated current density from corresponding EQE spectra; b) The average PCEs obtained from 5 independent devices.

Table S10. The photovoltaic parameters at different depths underwater of PBQx-TF:FPCC-Br-based devices.

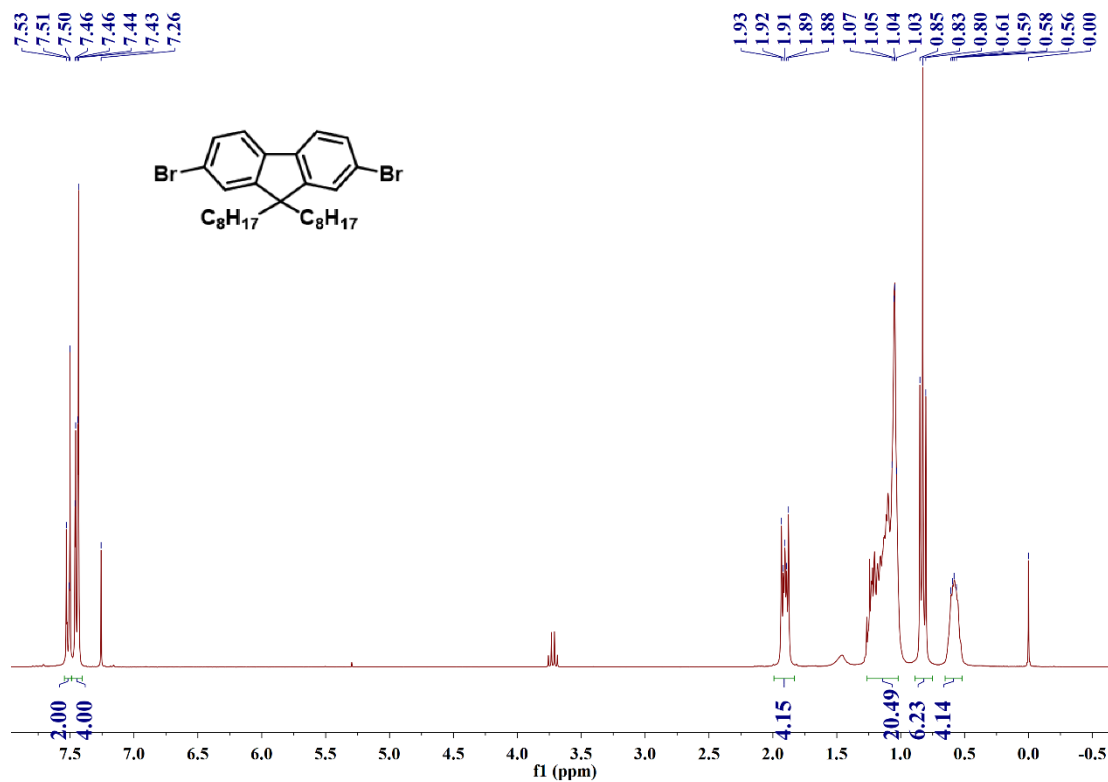
PBQx-TF:FPCC-Br	V_{oc} [V]	J_{sc} [mA cm^{-2}]	FF	PCE [%]
0 cm	1.063	16.3	0.749	13.0
1 cm	1.066	16.4	0.748	13.0
3 cm	1.067	16.1	0.752	12.9
5 cm	1.067	16.0	0.751	12.8
10 cm	1.062	15.6	0.750	12.4

Table S11. The photovoltaic parameters of two PBQx-TF:FPCC-Br-based cells

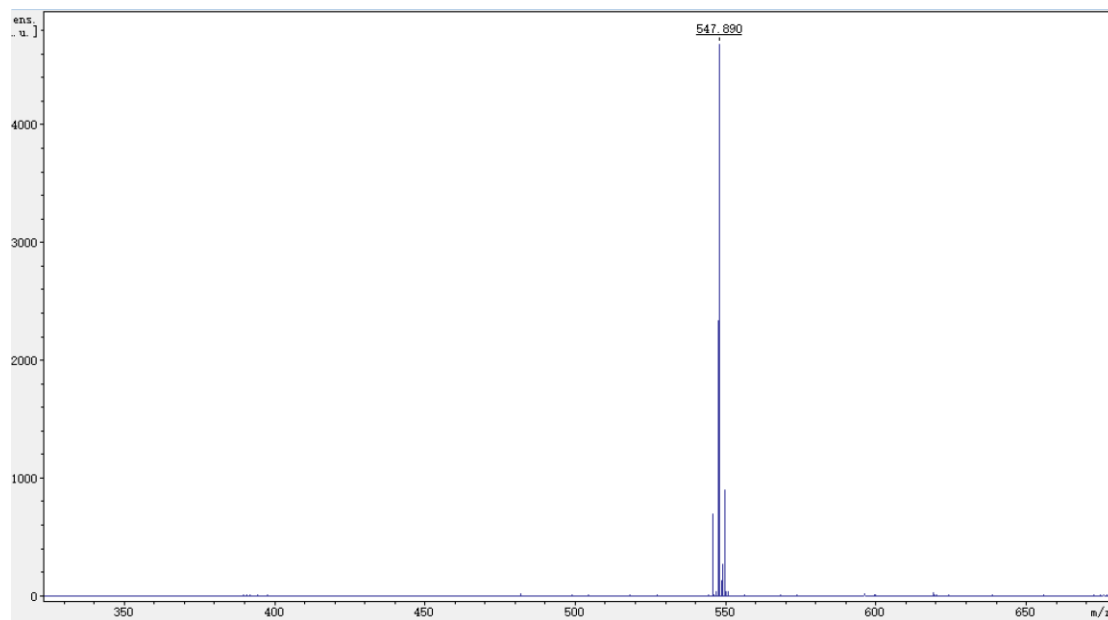
connected in series under AM 1.5 G and 5 cm underwater testing conditions.

conditions	V_{oc} [V]	J_{sc} [mA cm ²]	FF	PCE [%]
AM 1.5 G	2.16	7.90	0.697	11.9
5 cm underwater	2.17	7.55	0.708	11.6

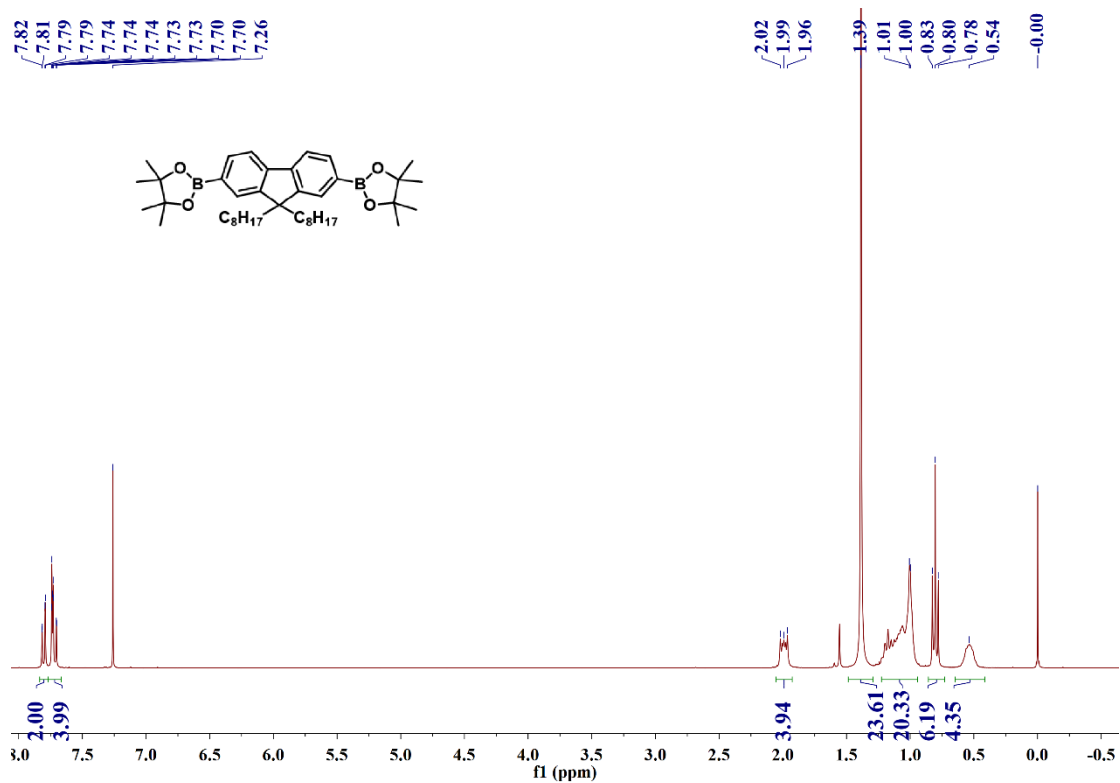
Supplementary NMR and MALDI-TOF figures.



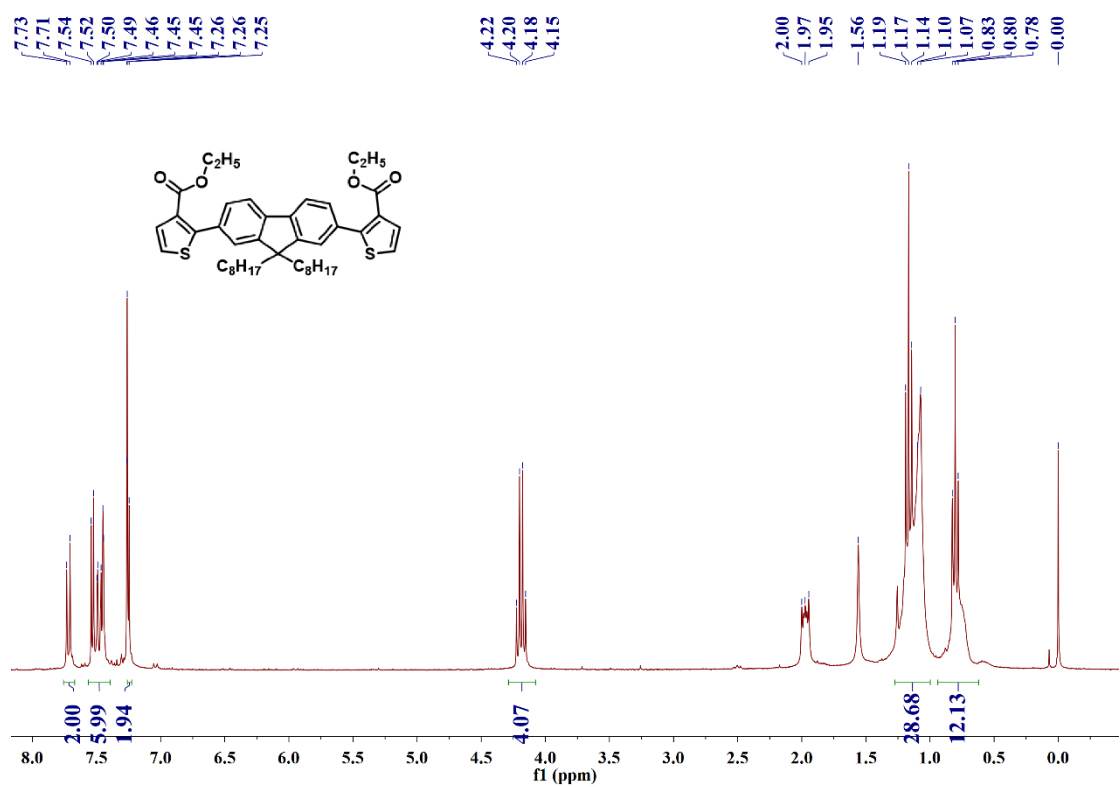
¹H-NMR spectrum of compound 2 in CDCl₃.



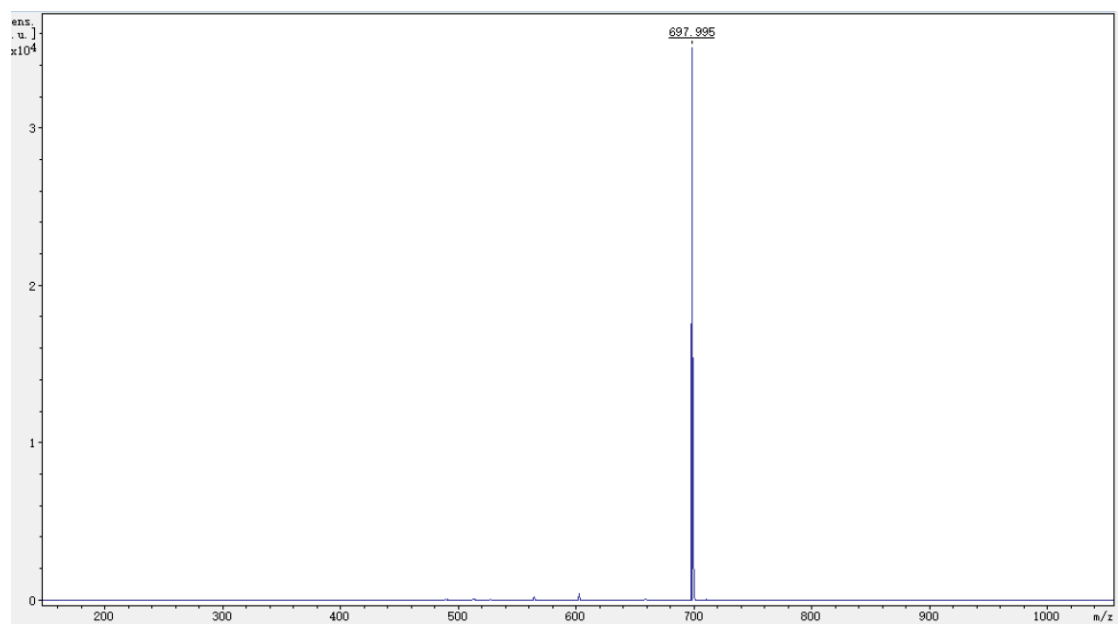
MALDI-TOF spectrum of compound 2.



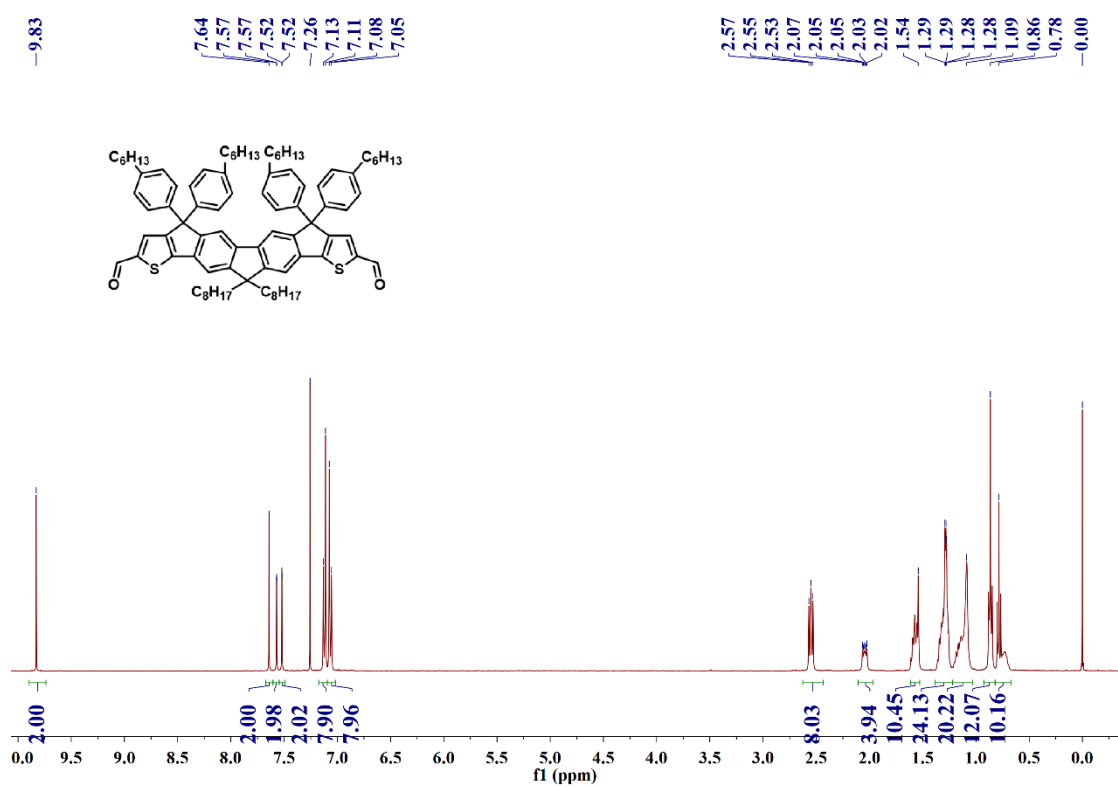
¹H-NMR spectrum of compound 3 in CDCl₃.



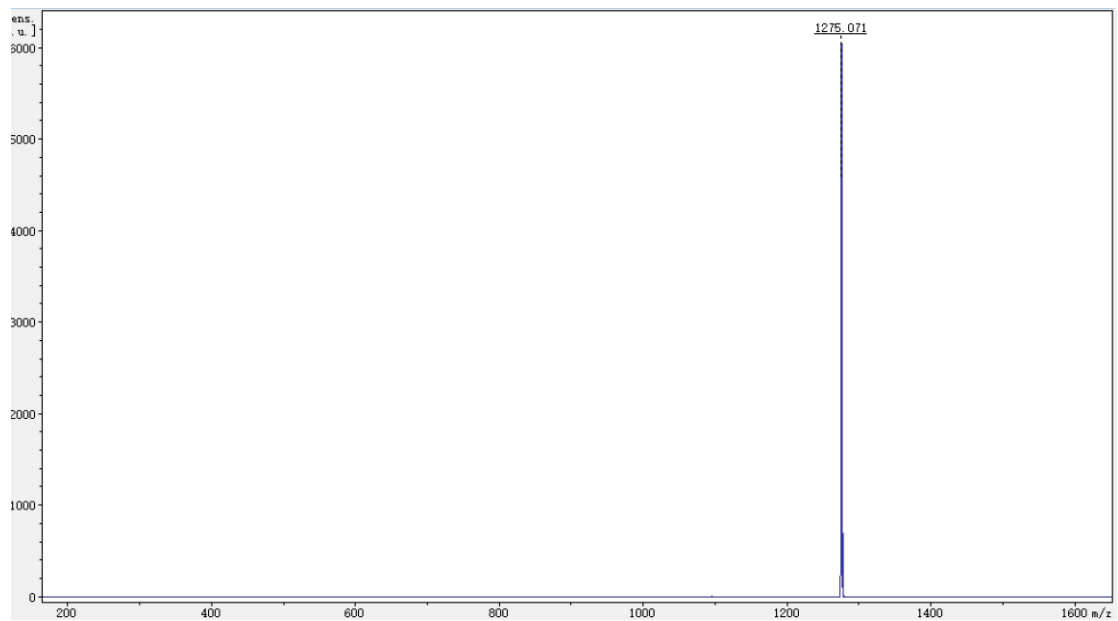
¹H-NMR spectrum of compound 4 in CDCl₃.



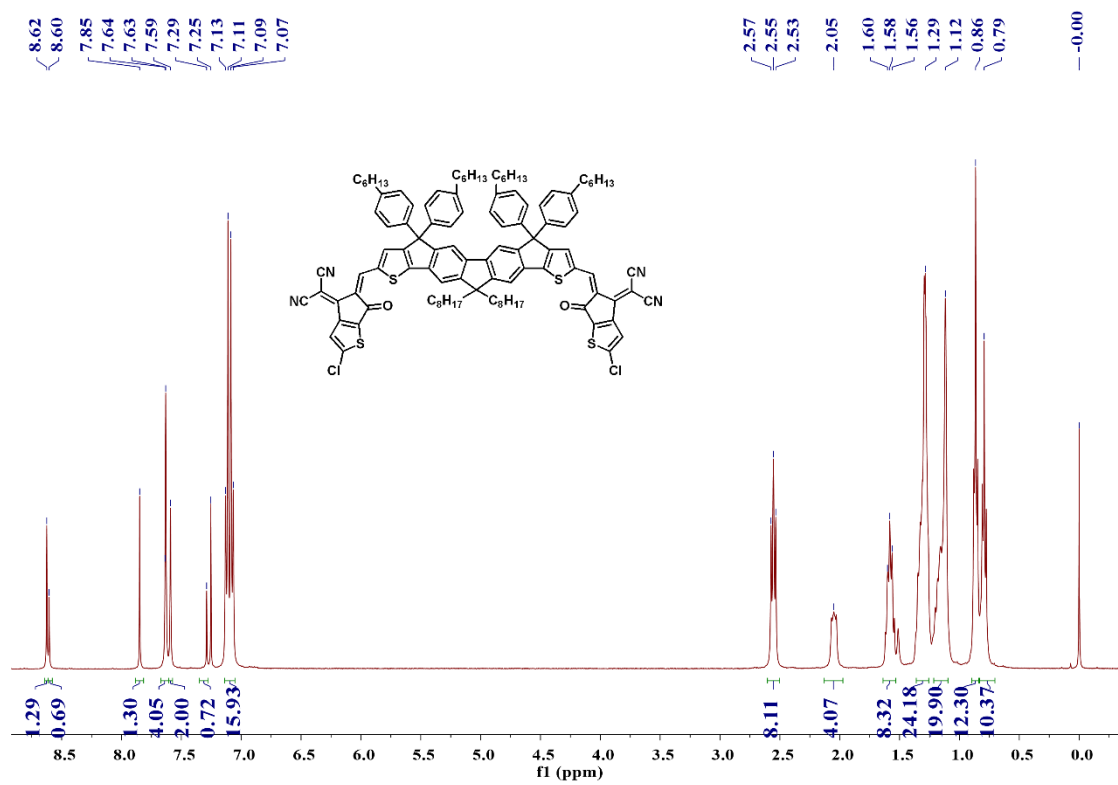
MALDI-TOF spectrum of compound 4.

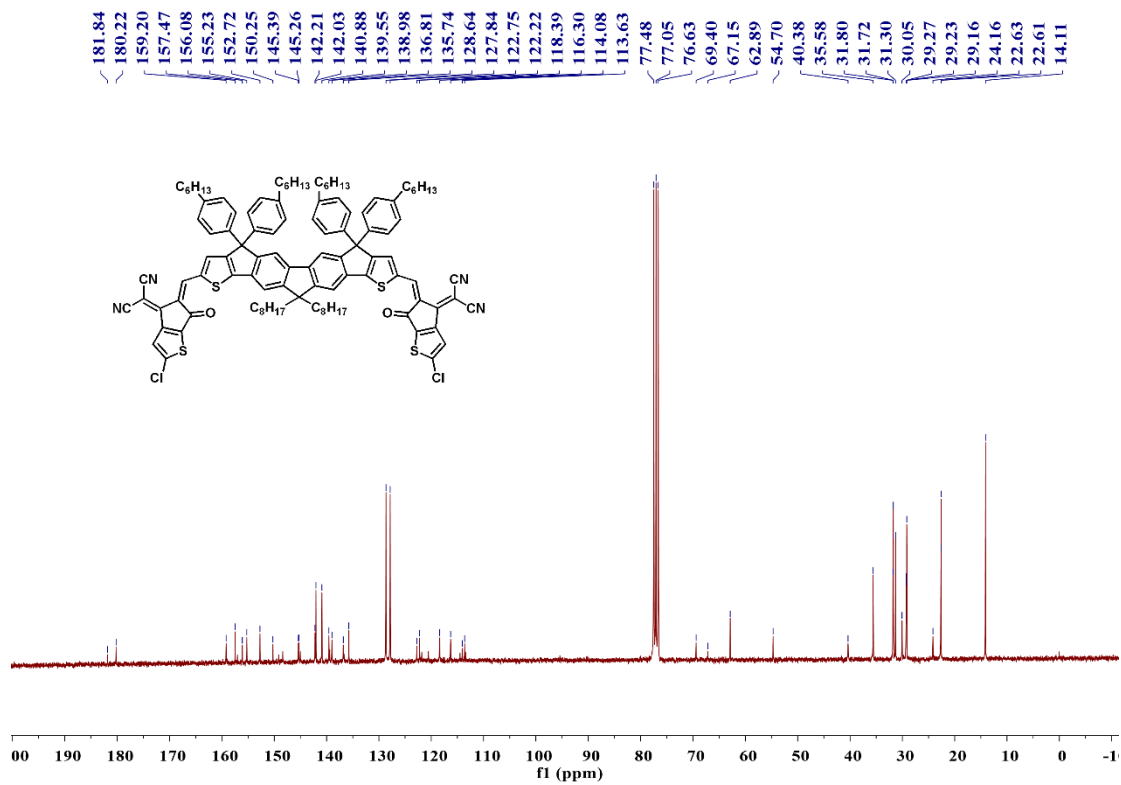


^1H -NMR spectrum of compound 5 in CDCl_3 .

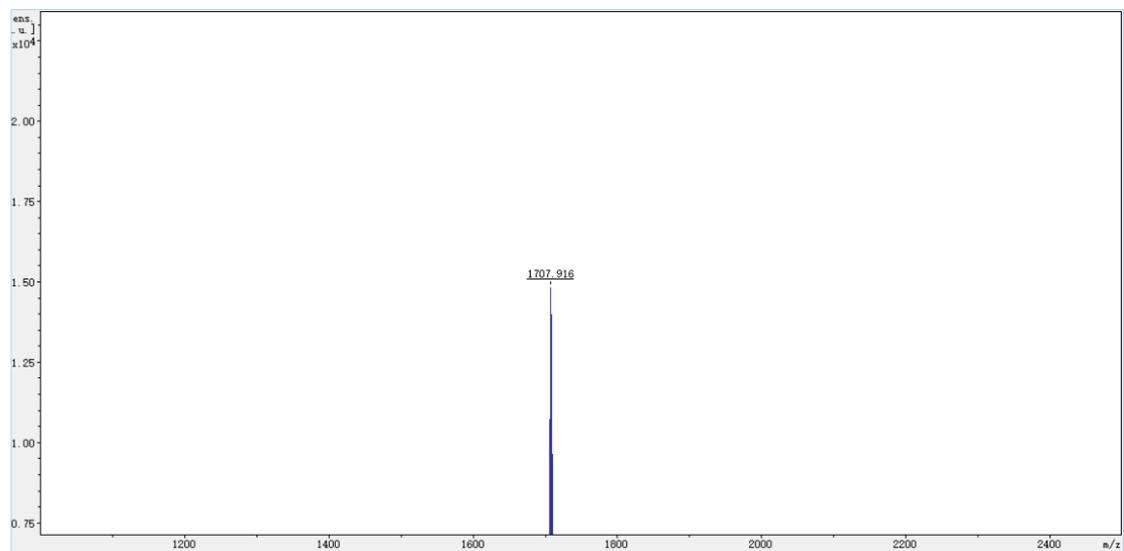


MALDI-TOF spectrum of compound 5.

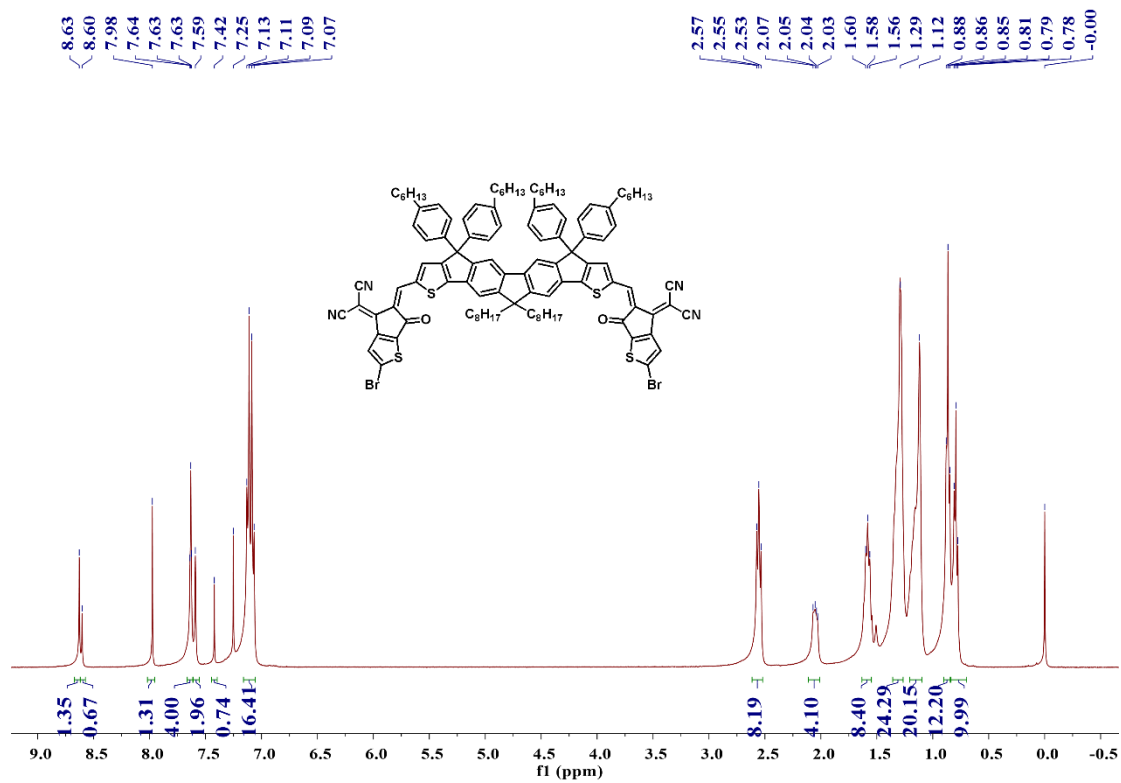




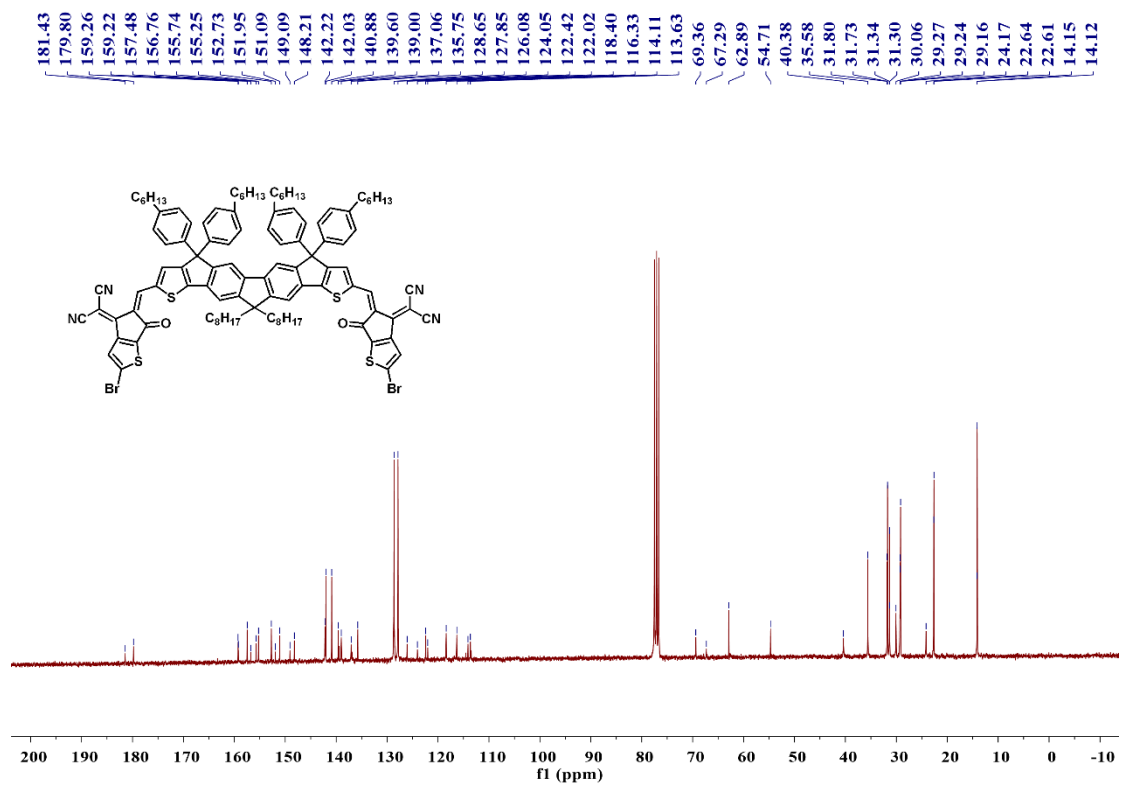
¹³C-NMR spectrum of FPCC-Cl in CDCl₃.



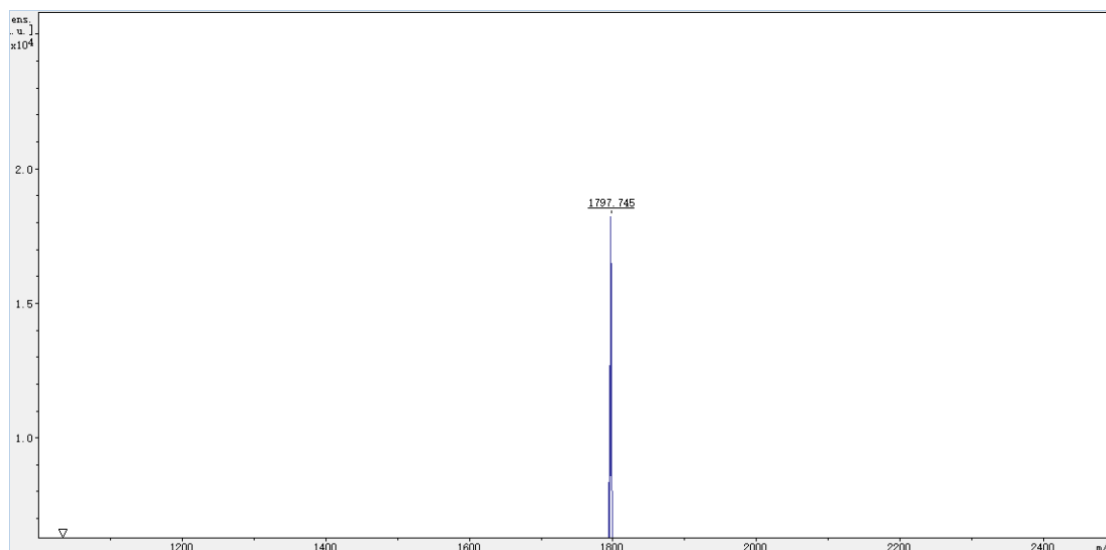
MALDI-TOF spectrum of FPCC-Cl.



¹H-NMR spectrum of FPCC-Br in CDCl₃.



¹³C-NMR spectrum of FPCC-Br in CDCl₃.



MALDI-TOF spectrum of FPCC-Br.

References:

- [1] S. Luo; F. Bai; J. Zhang; H. Zhao; I. Angunawela; X. Zou; X. Li; Z. Luo; K. Feng; H. Yu; K. S. Wong; H. Ade; W. Ma; H. Yan, *Nano Energy*, **2022**, *98*, 107281.
- [2] J. Zhang; Y. Li; H. Hu; G. Zhang; H. Ade; H. Yan, *Chem. Mater.*, **2019**, *31*, 6672.
- [3] T. Dai; A. Tang; J. Wang; Z. He; X. Li; Q. Guo; X. Chen; L. Ding; E. Zhou, *Macromol Rapid Commun*, **2022**, *43*.
- [4] Y. Cui; Y. Xu; H. Yao; P. Bi; L. Hong; J. Zhang; Y. Zu; T. Zhang; J. Qin; J. Ren; Z. Chen; C. He; X. Hao; Z. Wei; J. Hou, *Adv. Mater.*, **2021**, *33*, e2102420.
- [5] Y. Xu; Y. Cui; H. Yao; T. Zhang; J. Zhang; L. Ma; J. Wang; Z. Wei; J. Hou, *Adv. Mater.*, **2021**, *33*.
- [6] A. Tang; B. Xiao; Y. Wang; F. Gao; K. Tajima; H. Bin; Z. G. Zhang; Y. Li; Z. Wei; E. Zhou, *Adv. Funct. Mater.*, **2017**, *28*, 1704507.
- [7] T. Dai; Q. Nie; P. Lei; B. Zhang; J. Zhou; A. Tang; H. Wang; Q. Zeng; E. Zhou, *ACS Appl. Mater. Interfaces*, **2021**, *13*, 58994.
- [8] T. Zhang; C. An; Y. Xu; P. Bi; Z. Chen; J. Wang; N. Yang; Y. Yang; B. Xu; H. Yao; X. Hao; S. Zhang; J. Hou, *Adv. Mater.*, **2022**, *34*.
- [9] P. Bi; S. Zhang; J. Ren; Z. Chen; Z. Zheng; Y. Cui; J. Wang; S. Wang; T. Zhang; J. Li; Y. Xu; J. Qin; C. An; W. Ma; X. Hao; J. Hou, *Adv. Mater.*, **2021**, *34*.
- [10] D. Sun; D. Meng; Y. Cai; B. Fan; Y. Li; W. Jiang; L. Huo; Y. Sun; Z. Wang, *J. Am. Chem. Soc.*, **2015**, *137*, 11156.
- [11] Y. Lin; T. Li; F. Zhao; L. Han; Z. Wang; Y. Wu; Q. He; J. Wang; L. Huo; Y. Sun; C. Wang; W. Ma; X. Zhan, *Adv. Energy Mater.*, **2016**, *6*.
- [12] Y. J. Hwang; H. Li; B. A. E. Courtright; S. Subramaniyan; S. A. Jenekhe, *Adv. Mater.*, **2015**, *28*, 124.
- [13] Y. Fu; B. Wang; J. Qu; Y. Wu; W. Ma; Y. Geng; Y. Han; Z. Xie, *Adv. Funct. Mater.*, **2016**, *26*, 5922.
- [14] C. Zhang; T. Liu; W. Zeng; D. Xie; Z. Luo; Y. Sun; C. Yang, *Mater. Chem. Front.*,

2017, 1, 749.